Erik Josberger

Proton Conducting Devices and Materials

Erik Josberger

A dissertation

submitted in partial fulfillment of the

requirements for the degree of

Doctor of Philosophy

University of Washington

2016

Reading Committee:

Marco Rolandi, Chair

Karl Bohringer

Manjari P. Anantram

Program Authorized to Offer Degree:

Electrical Engineering

University of Washington

Abstract

Proton Conducting Devices and Materials

Erik Josberger

Chair of the Supervisory Committee:
Affiliate Associate Professor Marco Rolandi
Department of Materials Science and Engineering

The flow of protons is vital in biology, driving natural processes like the production of adenosine triphosphate (ATP) (*1*). Micro-scale fluctuations in pH can provide insight into neural activity and regulate cellular activity (*3, 4*), and antibiotics like gramicidin destroy cells by conducting protons across a cell membrane (*2*). However, modern electron-based devices are forced to use only the subset of biochemical reactions that can be controlled by electron motion. I have researched a broad variety of protonic systems, with the aim of enabling a direct interface between protons and electrons. Throughout, I utilize palladium hydride (PdH) as a proton-electron transducer. In this work, I present my efforts to measure and control the flow of protons. I have developed a protonic toolset, with devices ranging from complementary transistors to depletion-based memory devices. In addition, I present new understandings of the PdH-material interface, and characterize a novel protonic material. In addition, I describe initial efforts to create artificial carbon nanotube based protonic devices. These results represent new opportunities for the measurement and control of protons in bioelectronics.

TABLE OF CONTENTS

LIST OF FIGURES

ACKNOWLEDGEMENTS

I gratefully acknowledge everyone who has helped me on this journey. My thanks go to Marco, for his insightful guidance and the opportunities he gave me. Thank you to Yingxin, who made protonics possible, and thank you to Takeo, Zahra, Pegah, Xiaolin, Scott, Rylan, Wei, and Jungho for their assistance as colleagues and friends. Thank you also to my committee members for their time and considerate feedback. Thank you to Andy, Darick, and the WNF staff for sharing their extensive expertise in wafer fabrication

I would like to thank my funding agencies for their financial support: the National Science Foundation CAREER award (DMR 1150630), the U.S. Department of Energy Office of Science Award # <DE-SC0010441>, and the Office of Naval Research Award # N00014-14-1-0724

To my parents, Ed and Berit, for their encouragement and guidance, and to my wife, Mary, for her love and support.

1. INTRODUCTION

1.1 The Potential of Protonics

Proton and ion conducting devices have the subject of considerable reseacrh in the last decade. These devices represent a new way to translate from the ionic language of biology to the electronic language of circuitry. After billions of years of evolution, natural systems possess incredible arrays of sophisticated chemical and electrical capabilities that frequently surpass modern engineering (*5*). As an example, the brain of a rat has an effective computational capacity of 78 teraflops, while the IBM Blue GeneL supercomputer has 92 teraflops – and rats are significantly cheaper (*6*).

Significant research has been devoted to the Organic Electrochemical Transistor (OECT) (*7*). These devices make use of PEDOT, an ion-conductive polymer. In the device, the electrostatically gated flow of ions into and out of a PEDOT channel changes the charge carrier density and device conductivity. Complementary doping of the PEDOT allows the creation of pn junction devices (*8*). The use of electrolyte solutions as source and drain electrodes allows the injection of these ions into specific regions of cell cultures, allowing the delivery of biochemical signaling molecules with 50μm accuracy (*9*).

Separately, carbon nanotubes (CNTs) have been used as sensitive bioelectronic sensors. In one demonstration, the Noy group covered a CNT with a lipid bilayer. Proton-pumping proteins are embedded in the layer, and when they are activated the resulting solution charge changes the surface charge of the CNT (*10*). Separately, the Noy group has demonstrated that CNTs can conduct protons, and might be used as artificial membrane pores (*11*).

In nature, protons serve myriad functions. The flow of protons across a mitochondrial membrane drives the production of ATP, the biological energy currency (*1*). Micro-scale fluctuations in pH can provide insight into neural activity and regulate cellular activity (*3, 4*). In turn, antibiotics like gramicidin destroy cells by rapidly conducting protons across a cell membrane (*2*). Several natural materials conduct protons, including melanin (*12*), reflectin (*13*), and bovine serum albumin (*14*). In particular, this thesis is built off of pioneering efforts by Chao Zhong, Yingxin Deng, and the Rolandi research group, who demonstrated the first protonic device (*15*), and I gratefully acknowledge their efforts. Nature's control of proton motion is admirable, and replicating it may open new frontiers for biomedical research.

2. BACKGROUND INFORMATION

2.1 The Grotthuss Mechanism for Proton Conduction

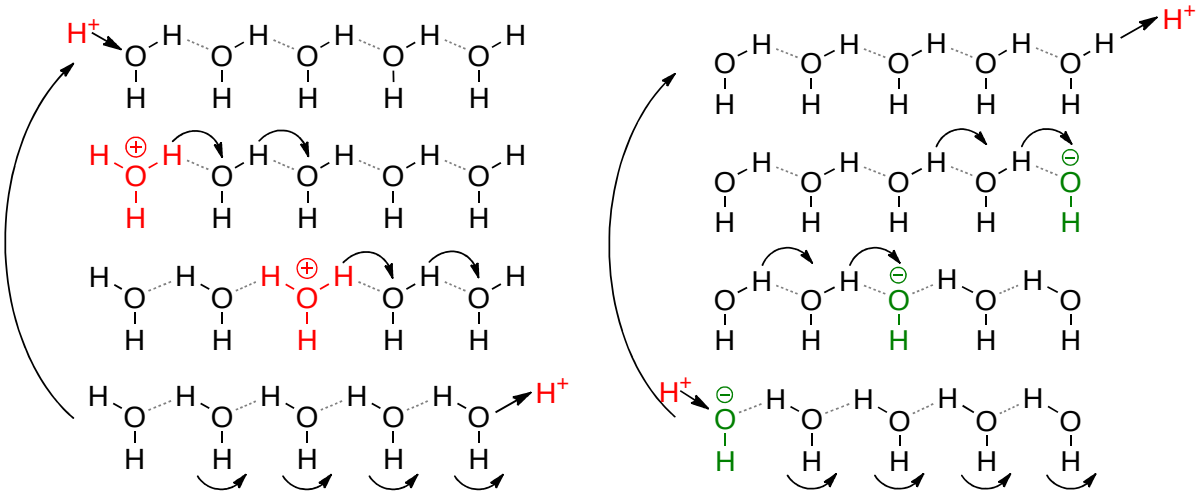

Figure 2.1.1. Protons conduct across chains of hydrogen-bonded water molecules ('water wires') through either of two mechanisms. Left: an extra H^+ attaches to an H_2O, forming H_3O^+. Under an applied bias, the hydrogen bond and covalent bond between adjacent molecules swap, effectively causing the H_3O^+ to move one molecule to the right – a single 'hop'. Repeated hops lead to continuous conduction. Before conducting another proton, a rotational step returns the wire to its initial state. Right: an H^+ detaches from an H_2O, leaving OH^-. Conduction then follows a similar hopping mechanism in the reverse direction.

Proton conduction in gramicidin or other water chains occurs by the Grotthuss mechanism. First proposed in 1806 by Theodor Grotthuss, this mechanism gives protons a conductivity 6-7 times higher than Na^+ in water (*16*). Protons in a bulk solution do not exist as free H^+, instead bonding with a water molecule to form H_3O^+. Most water molecules form hydrogen bonds with their two neighboring molecules. These hydrogen bonds can swap with the covalent bond of

the H_3O^+, transferring the extra proton to the neighboring molecule (Figure 2.1.1). Chains with an OH^- also conduct protons by a similar mechanism of hopping. In a solution, these networks are random, with only short-range ordering that is insufficient to allow rapid transit. However, the regular lattice of ice can provide the requisite long-range hydrogen bond networks for proton conduction as observed by Eigen and DeMaeyer (*17*). They model this system as a semiconductor, with H^+ and OH^- transport analogous to electron and hole transport in silicon.

2.2 Proton Conduction in Biomaterials

In aqueous solutions, the ordering of hydrogen bond networks does not have a long enough range to allow significant Grotthuss transfer. The effective diffusion constant for protons in bulk water is 40 times smaller than that of an ordered water chain (*18*). However, the regular structure of a long biopolymer allows the formation of a long-range hydrogen bond network connecting with the –OH groups on the polymer backbone (*19*) (Figure 2.2.1). As previously demonstrated in biopolymers like keratin and collagen, this allows for proton conduction by the Grotthuss mechanism at room temperature (*20, 21*). In addition, acid and base groups on the polymer can donate or accept protons from this solution, extending the semiconductor comparison from ice to include complementary doping.

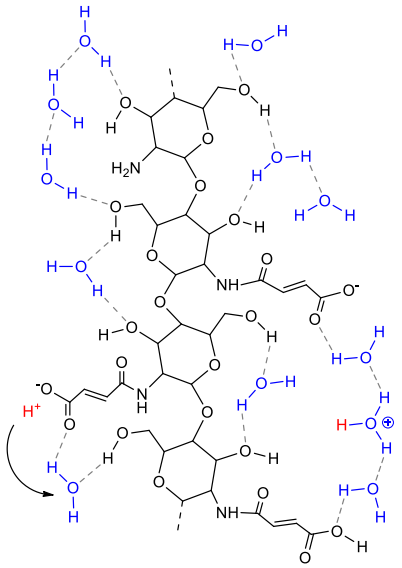

Figure 2.2.1. OH groups on a polymer provide a natural framework for the formation of a long-range hydrogen bond network. Water molecules are typically supplied from atmospheric hydration. Acid groups (-COOH termination) can act as proton donors.

2.3 Palladium Hydride as a Protonic Contact

Palladium Hydride (PdH_x) is a robust material that acts as a source of protons through the reaction (*22*):

$$PdH \rightarrow Pd + H^+ + e^- \qquad (2.3.1)$$

Here, a PdH unit splits into its constituent pieces at the surface of the PdH_x contact (Figure 2.3.1). The reaction injects an H^+ into the surrounding material, while the e^- travels back through the contact. Since the flow of H^+ and e^- is equal, measuring the e^- current with conventional electronics reveals the H^+ current in the channel. The process can support a steady-state current as long as hydrogen is resupplied by diffusion from the bulk material and absorption of hydrogen gas from the atmosphere.

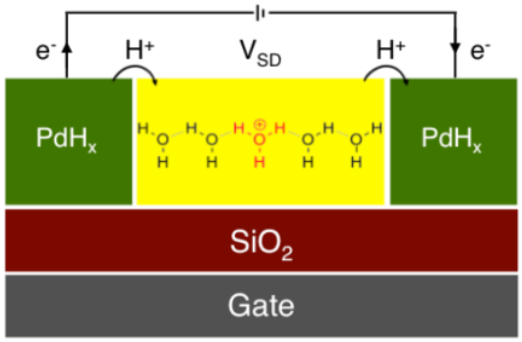

Figure 2.3.1. PdH can split into Pd, H^+, and e^-. The H^+ travels through the channel as protonic current. An equal e^- current travels through external circuitry, and is measured by conventional electronics.

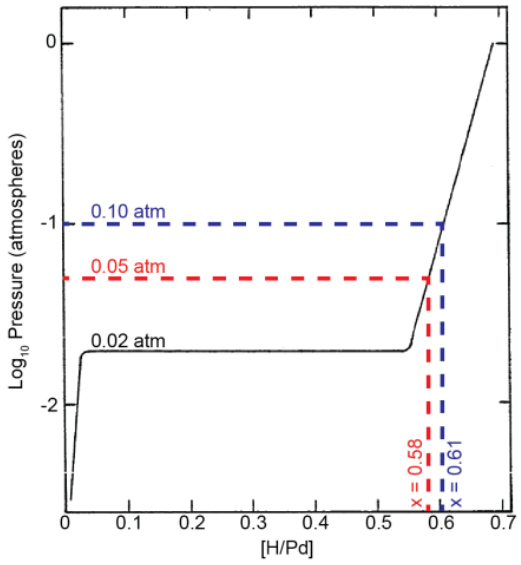

Figure 2.3.2. The applied partial pressure of hydrogen determines the stoichiometric ratio x of PdH_x (*23*). PdH_x transitions from an α phase to a β phase at p_{H2} = 0.02atm. After this transition, x is effectively stable with pressure: doubling the pressure from 0.05atm to 0.10atm increases x by only 0.03.

H in the bulk PdH_x is supplied by the absorption of hydrogen gas, H_2. A computerized gas control system supplies H_2 gas in a controlled ratio, typically at 5% relative concentration (p_{H2} =

0.05atm). The contacts begin as Pd, and naturally absorb the H_2 gas to form PdH_x. The partial pressure of H_2 sets the stoichiometric ratio x (*23*) (Figure 2.3.2). For pressures above 0.02atm, this equilibrium is inherently stable, with a pressure dependence of:

$$Log_{10}(p_{H2}) \approx 10 * [H/Pd] - 7.1 \qquad (2.3.2)$$

Standard metal evaporation and liftoff is used to fabricate these contacts. In this process, a lithographically patterned photoresist is coated with metal in an e-beam evaporator. Dissolving the photoresist leaves metal only where the photoresist was not present. Ultraviolet contact lithography allows 1µm photoresist features, while e-beam lithography allows for features as small as 10nm.

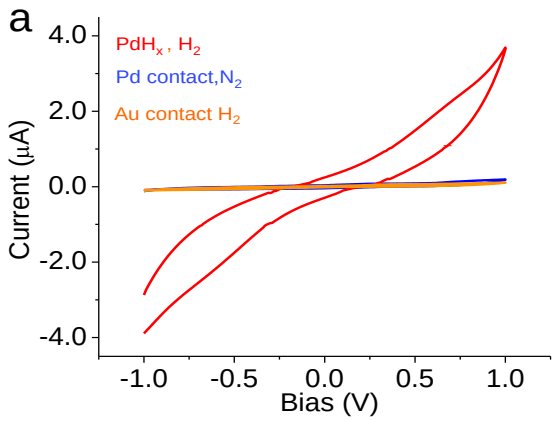

Figure 2.3.3. Two simple control experiments allow easy proof of proton conductivity (*15*). The electron conductivity of the sample is measured by removing the hydrogen gas to prevent the formation of PdH_x. Similarly, supplying only dry gas prevents the formation of water wires, eliminating the proton conductivity of Nafion and revealing any stray conduction paths.

PdH_x contacts also allow facile control experiments. H_2 is required for the contacts to supply a proton current, so excluding the gas allows the measurement of only the electron conductivity in a material (figure 2.3.3). To ensure that the hydrogen gas is not causing electron conductivity, I fabricated devices with Au instead of Pd. Au does not conduct protons, so any increase in current would indicate hydrogen-induced electron conductivity. Typically, I observe proton/electron current ratios greater than 400 (*15*).

3. RESEARCH TOPICS

3.1 High Protonic Current Density in Nafion Devices

Reproduced with permission from Advanced Materials

I have demonstrated that protonic devices with a Nafion channel can display memory behaviors that partially emulate the function of synapses in the brain. With the recent physical demonstration of memristive-based devices, (*24, 25*) low-power two terminal devices with memory (*26*) and learning functions have advanced electronics and neuromorphic computing (*27-32*). In neuromorphic computing, CMOS and transistor circuits (*33-35*) are designed to mimic architectures in the brain and synaptic connections between neurons whose conductivity is influenced by prior events (*36*). In memristive devices, typically slow moving ions are coupled with fast moving electrons (*37, 38*). Ionic motion affords memory, with electronic current as the output signal (*38*). In this work, I introduce fully ionic two- terminal devices in which protons provide both memory and output signal. These devices exhibit synaptic-like reversible short-term depression, device memory, and are turned “ON” and “OFF” with as little as 30 nJ of energy per bit.

In a chemical synaptic connection, neurotransmitters are released from the pre-synaptic neuron into the synaptic cleft upon arrival of an action potential (Figure 3.1.1a). These neurotransmitters diffuse across the synaptic cleft, couple with the receptors in the post-synaptic neuron, and trigger a subsequent action potential in the post-synaptic neuron. After firing, the pre-synaptic neuron runs out of neurotransmitters to release into the synaptic cleft upon the arrival of a subsequent action potential. As a consequence, the action potential is not transmitted to the post-synaptic neuron. This temporary interruption of the synaptic

connection is referred to as short -term depression (STD) (*36*). STD is an important form of signal modulation in the brain.(*39*) In the protonic two-terminal device (Figure 3.1.1b, c), palladium hydride (PdH_x) source and drain contacts inject and drain protons (H^+) into and from the Nafion. (*15, 22, 40, 41*) For each H^+ injected into the Nafion, an excess electron is collected by the leads, which complete the circuit. The source and drain contacts in the protonic two-terminal devices are analogous to the pre- and post- synaptic neurons in a chemical synapse. Nafion is a proton-conducting and electron insulating polymer widely used as proton exchange membrane in fuel cells, with a proton conductivity of 0.078 S cm^{-1} (*42-44*). An applied voltage (V_{SD}) causes an H^+ current (I_{SD}) to flow between source and drain contacts in the protonic device (Figure 3.1.1d). This current depletes hydrogen from the PdH_x source wherever it is in direct contact with the Nafion. This depletion creates a hydrogen concentration gradient in the PdH_x and a subsequent diffusion flux inside the contact. For low current densities, the diffusion flux in the PdH_x, the absorption of hydrogen from the H_2 atmosphere, and I_{SD} balance out and the PdH_x contacts effectively function as protodes -- the protonic equivalent of electrodes (*15, 22, 40, 41*). For higher current densities, as in the Nafion channel, a region of the source contact fully depletes of hydrogen to form Pd. Pd can no longer inject H^+ in the Nafion and I_{SD} decays as a function of time. As a result, a V_{SD} pulse produces a spike in I_{SD} as the contact depletes (Figure 3.1.1d). This type of transient behavior has previously been observed in PdH_x reversible electrodes in contact with an acidic solution (*45*).

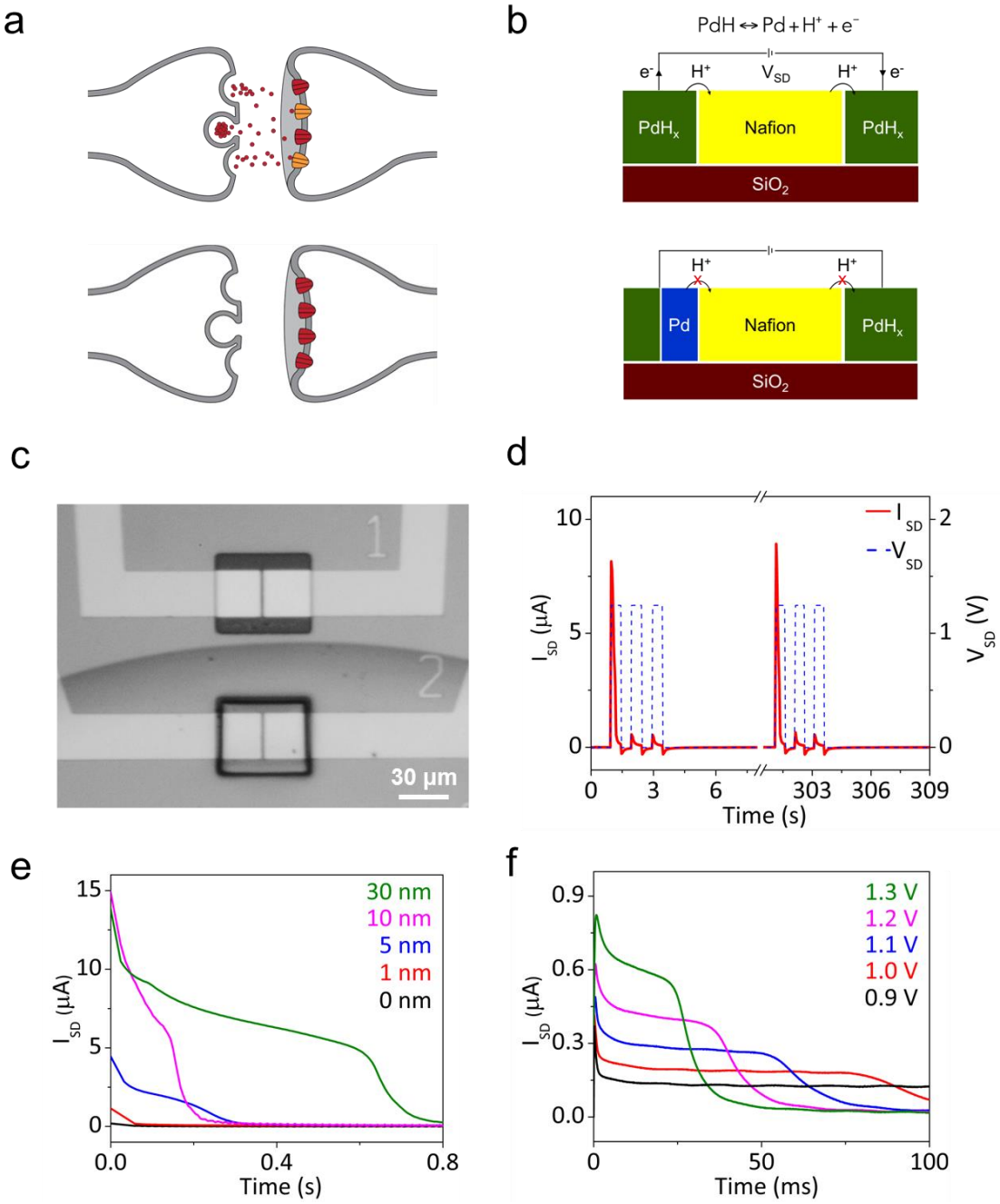

Figure 3.1.1. Synaptic behavior of protonic devices. (a) Synaptic transmission in a chemical synapse. Orange neurotransmitter receptor ion channels are open due to binding of released neurotransmitters. (b) Protonic device. A voltage (V_{SD}) is applied across two PdH_x contacts separated by proton conducting Nafion. A H^+ current (I_{SD})

flows from the source (left) to the drain (right). This H^+ current depletes the PdH_x source of hydrogen to form Pd (not proton conducting) and the protonic device is depleted. (c) Microscope image of a PdH_x-Nafion protonic device. Lithographically patterned source and drain contacts 30 μm wide are separated by a 1 μm gap. In device (f), the Nafion deposition on the source contact is limited to an area 11μm x 30 μm with SU-8. (d) Plot of current (I_{SD}) as a function of time for a protonic device 30 μm wide by 500 μm long (e) Current spike behavior (V_{SD}= 1 V) for protonic devices as a function of PdH_x contact thickness. (f) I_{SD} dependence on V_{SD} and I_{SD} at t = 0s. Contact is 10 nm thick PdH_x.

The reduction in signal transmission strength after a pulse for the protonic device closely resembles the short-term depression (STD) plasticity of a biochemical synapse. In a biochemical synapse, depletion of neurotransmitters from the presynaptic neuron results in no signal transmission across the synaptic cleft. Here, in close analogy to the biochemical synapse, depletion of hydrogen from the PdH_x source results in no H^+ current across the device upon arrival of a subsequent voltage pulse. Similarly to STD, waiting a determined period of time (300 s) restores the initial behavior as the source contact replenishes hydrogen from the atmosphere. To corroborate this picture, I fabricate protonic devices with PdH_x contacts of varying thicknesses (Figure 3.1.1e). Thinner contacts deplete faster than thicker ones due to an overall lower amount of hydrogen available in the PdH_x to be injected in the Nafion as H^+. Thicker contacts (30 nm and 10 nm) result in comparable device I_{SD}, while 5 nm PdH_x contacts show lower I_{SD} most likely due to reduced contact quality. Contacts with an equivalent thickness of Au, but no PdH_x (0 nm), result in little or no current as expected. As discussed in

section 2.3, Au is an excellent electronic conductor for source and drain contacts, but cannot inject H^+ into the Nafion. A protonic device with limited contact area between the PdH_x and the Nafion (Figure 3.1.1f) affords switching speeds of 25 ms with an on-off ratio of approximately 100. The switching speed of the protonic device is comparable to the switching speed of a biological synapse (*46*). The switching speed depends on V_{SD}. For a Nafion channel with fixed resistance, a larger V_{SD} results in higher I_{SD} and faster source contact depletion (t_{spike}). In these devices, V_{SD} is limited to ≤ 1.3 V to avoid water electrolysis. For a given contact volume, I assume that the PdH_x source contains a fixed amount of H and the contact is fully depleted when all of the H travels across the device channel as H^+. To confirm this observation, the total amount of charge (Q) flowing across the Nafion channel during an I_{SD} spike is calculated as

$$Q = \int_{t=0}^{t=t_{spike}} I_{SD}\,dt \qquad \text{(eq. 3.1.1)}$$

Integrating I_{SD} as a function of time gives the total number of H^+ ions that flow across the channel, and therefore the total number of H atoms stored in the contact. The measured Q is constant as a function of V_{SD} and increases with PdH_x thickness. The conservation of charge as calculated in Equation 3.1.1 means that a larger I_{SD} results in a shorter t_{spike}. For the same V_{SD}, I_{SD} depends on channel resistance, which is linearly depended on channel length. A device with a 3 µm channel length has I_{SD} = 4 µA and t_{spike} =1.5s, while an equivalent device with a 1 µm channel has I_{SD} =15 µA and t_{spike} = 0.6 s. Devices with a shorter channel, and thus lower channel resistance, are expected to show a higher I_{SD} for the same V_{SD}, and a faster t_{spike}. Overall, the STD behavior observed in the two-terminal protonic devices (Fig. 3.1.2d) is qualitatively similar to the STD behavior of a chemical synapse. Chemical synapses, however, also exhibit short-term potentiation and resulting spike timing dependence, which are both important for signal

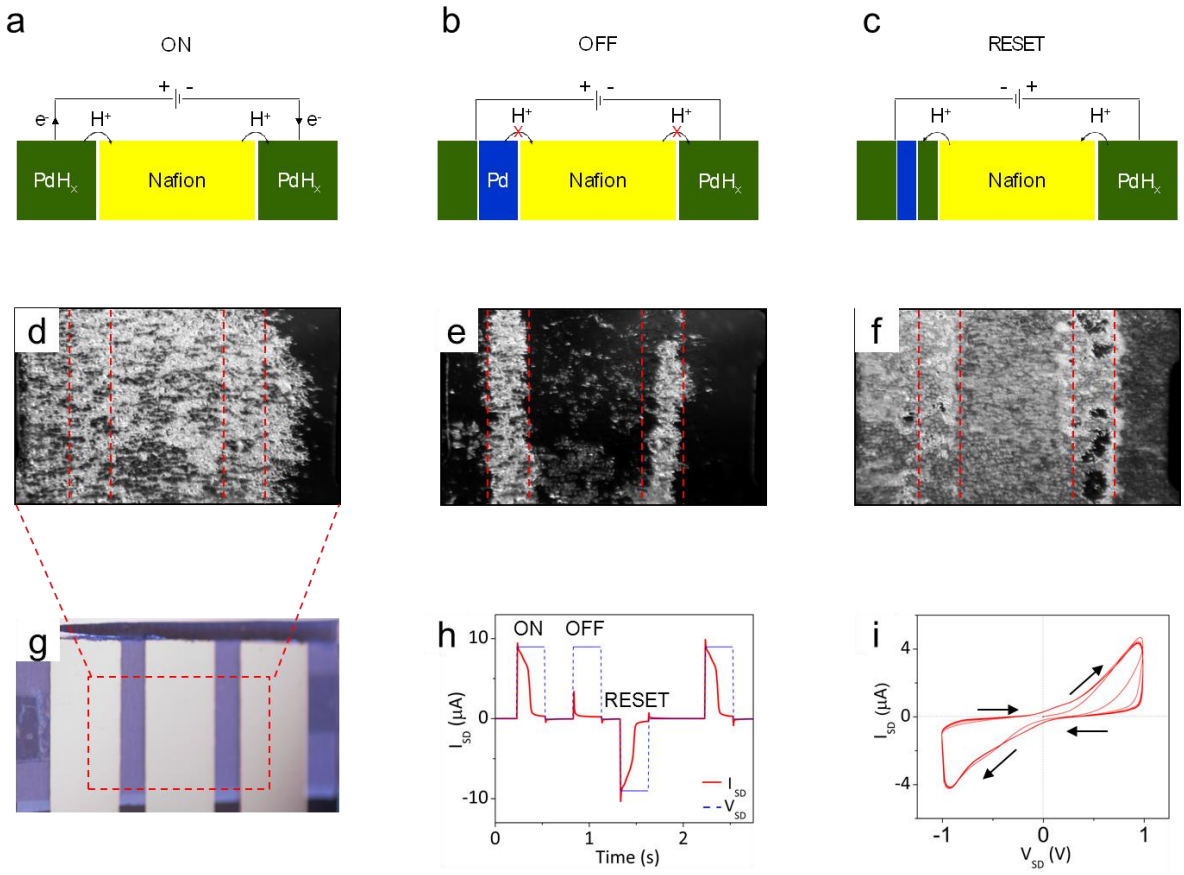

Figure 3.1.2. Memory behavior of a protonic device. (a), (b), (c) Schematic side views of protonic devices showing proton depletion and reuptake in the source contact. (a) ON state. (b) OFF state after a V_{SD} pulse and resulting I_{SD} spike depletes the PdHx source of hydrogen to form Pd. (c) RESET. A negative V_{SD} injects H^+ back into the source to form PdHx and restores the devices from depression. (d), (e), (f), (g) Optical images of a PdH_x source in a sandwich device fabricated on glass. Lighter areas are PdH_x and darker areas are Pd. (d) V_{SD} = 0 V. (e) V_{SD} =1.25 V. (f) V_{SD} = -1.25 V. (h) Demonstration of ON and OFF switching in an analogous micro device. Three positive SET pulses (V_{SD} =1.25 V, 0.25 s) and a negative RESET pulse (V_{SD} = -1.25 V, 0.25 s) were applied. (i) I-V curve for a micro device, showing the hysteresis in the PdH_x-Nafion system.

transmission in the brain (*39*). Short-term potentiation and spike timing dependence are not observed in the present configuration and are not the focus of this work, but may be achieved in the future by pre-loading H in the PdH_x source with a V_{SD} pulse.

In this work, I instead focus on the potential of creating a two-terminal device memory with reconfigurable "ON" and "OFF" states (Figure 3.1.2). A protonic memory in the ON state (Figure 2a) conducts I_{SD} continuously with a small V_{SD} applied (Figure S3). A positive V_{SD} = 1.25 V turns the protonic memory OFF (Figure 2b). A reverse V_{SD} = -1.25 V injects H^+ back into the source contact to reform PdH_x and RESETs the memory to the ON state (Figure 2c). To observe this process, I fabricate sandwich devices on transparent glass supports and image the source contact in the different memory states under an optical microscope (Figure 2 d, e, f, g) (*47*). Upon hydrogen absorption from the H_2 atmosphere, the source contact changes color from metallic Pd to white PdH_x (Figure 3.1.2d). A positive V_{SD} pulse depletes the PdH_x of hydrogen, and the PdH_x returns to metallic Pd as seen in the OFF state device (Figure 3.1.2e). When the device is RESET, hydrogen is loaded as H^+ from the Nafion channel back into the source contact to form white PdH_x (Figure 3.1.2f). This reloading is analogous to reuptake in neuronal synapses, which can actively pump the unused neurotransmitter back into the presynaptic neuron for reprocessing and re-release following a later action potential (*39, 48*). Memory cycling is demonstrated from the I_{SD} output of a protonic device (Figure 3.1.2h) with the same structure as the one described in Figure 3.1.1. The magnitude and the time duration of the I_{SD} spike resulting from the RESET V_{SD} pulse are the same as the magnitude and the time duration of the I_{SD} spike for the ON-OFF V_{SD} pulse. This signifies that a fixed amount of hydrogen is shuttled between the source and drain contacts in the form of an H^+ current in the Nafion (I_{SD}). It is likely

that the ON-OFF cycle does not increase the concentration of H in the drain contact to x> 0.6. As described in equation (2.3.2), the equilibrium pressure of H_2 increases exponentially when x is larger than 0.6 (*23*). It is therefore likely that additional hydrogen added to a contact that already has x=0.6 diffuses into the atmosphere instead of increasing the hydrogen loading of the PdH_x. Cycling the protonic device by applying a 2 Hz, 1 V sine wave to V_{SD} confirms the device characteristics with a clear hysteresis between the ON and OFF states (Figure 3.1.2i). I_{SD} is the same in either direction, which is similar to unipolar resistive switching (*49*). Cycling is performed 22 times, indicating reasonable reproducibility. For V_{SD}= 0 V and increasing, the device is in the ON state, turning OFF at up to V_{SD}= 1V. In the OFF state, the source contact is fully depleted of H and is no longer capable of injecting H^+ into the Nafion channel. The device stays OFF for V_{SD}> 0 until the polarity of V_{SD} is reversed. A device in the OFF state for V_{SD}> 0 V is in the ON state for V_{SD} < 0 V, because the PdH_x drain contact is not depleted of H. A V_{SD}< 0 V depletes the drain contact of H and the device eventually turns OFF for V_{SD} = -1 V. At the same time, V_{SD} < 0 V moves H^+ back into the source contact. This replenishes the H in the PdH_x source and puts the device is in the ON state for V_{SD} > 0 V. The state of these devices is governed by the amount of charge flux that has gone through the device, specifically the amount of H^+ that is shuttled back and forth in the Nafion channel. As such, these protonic devices have similar characteristics to memristors with the charge flux being the state variable (*24, 25*). In these devices the protons both regulate the state of the device and provide the output signal, unlike most memristors where ions control the state of the device and electrons are the output signal (*24, 25*). However, in these protonic devices the hysteresis loop is not pinched with zero crossing, as is characteristic of memristors. The behavior of the protonic

devices can be qualitatively described as two memristive diodes (the source and drain contacts) arranged back to back. However, further work is necessary to develop a full analytical description of the device characteristics, some portion of which is described in section 3.4.

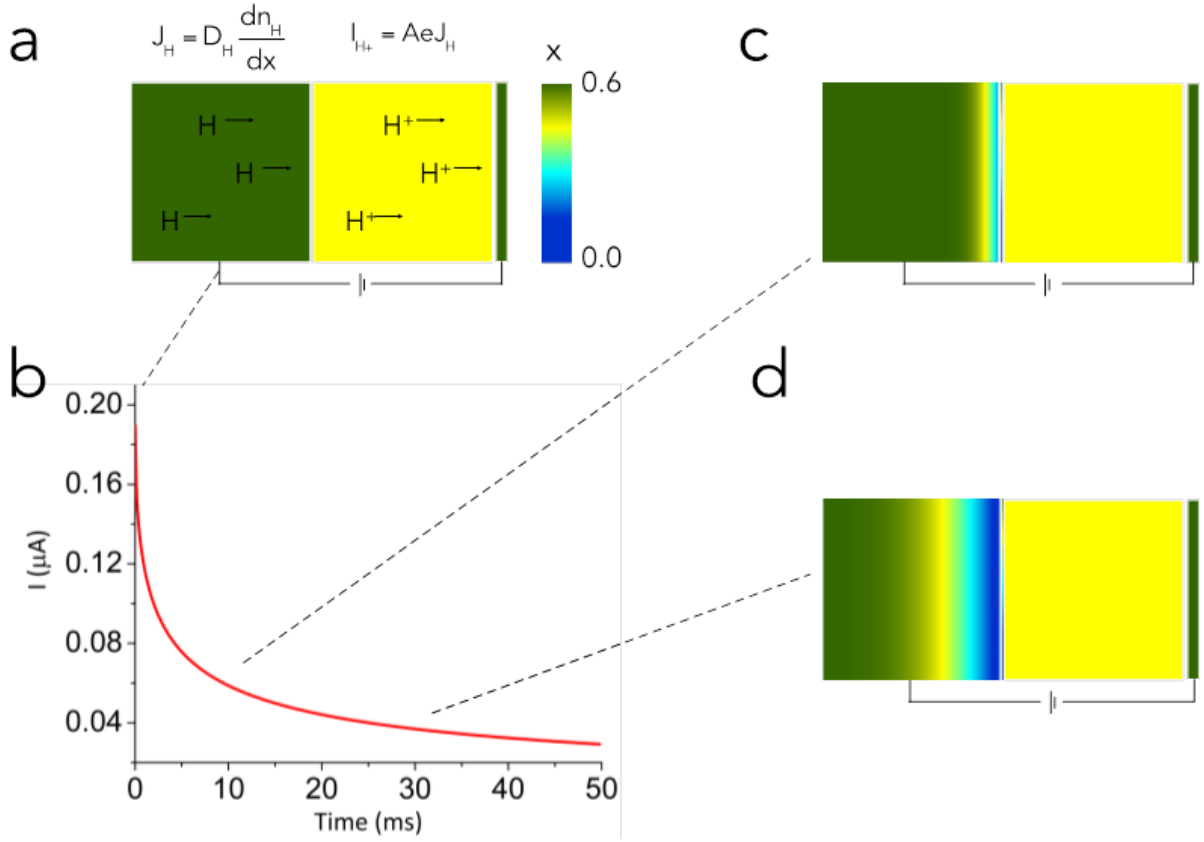

Figure 3.1.3. Protonic device modeling. (a) Simplified schematic of the device for simulation. (b) Device current. (c), (d) Simulated H concentration for PdHx source for t=5 ms, and t=50 ms respectively. For t=0s, x is set to 0.6 throughout the contact.

To better illustrate the workings of protonic devices, I developed a simple one-dimensional physical model (Figure 3.1.3). In this model the diffusion flux (J_H) of hydrogen inside the PdH_x contact follows Fick's first law of diffusion and conservation of mass. For this simple model, I neglect any exchange of hydrogen between the PdH_x and the surrounding H_2 atmosphere.

Assuming continuity across the PdH_x Nafion boundary, I postulate that the current of H^+ in the Nafion channel (I_{SD}) is equal to J_H in the last PdH_x cell in contact with the Nafion times the charge of a proton (e) and the contact area of the device (A). Therefore, the hydrogen diffusion in the PdH_x is driven by the induced electric drift of H^+ from the contact-Nafion interface and along the Nafion channel, in a fashion similar to the transfer of H^+ to an acidic water solution in the palladium hydrogen reversible electrode (*45*). This model does not include any trap states, (*45*) or the accurate 2D device geometry, which likely affect the I_{SD} characteristics in the experimental protonic devices. Nonetheless, by setting I_{SD}= 0.2 μA for t=0 I reproduce a I_{SD} time dependence (Figure 3.1.3c) that is consistent with the experimental results of the faster protonic devices (Figure 3.1.1f). This model provides insights in the spatial dependence of the hydrogen concentration (x) in the PdH_x - source contact (Figure 3.1.1c, d) at different time points. As expected, a hydrogen-depleted region of Pd grows with time in the source contact and results in a smaller I_{SD} when the device is eventually turned from the ON to the OFF state. Further refinement of this model is necessary to quantitatively replicate the full device characteristics. A consequence of the simple diffusion based characteristics of the protonic devices is the potential for ultra-low power computing. Current devices (Figure 3.1.1f) with micron size contacts are limited to *ca.* 30 nJ of energy per switching event, based on the amount of hydrogen stored within the contact. I estimate that a protonic memory device with 20 nm wide contacts may use as little as 30 fJ per operation, which is two orders of magnitude smaller than the energy used by a natural synapse (1pJ).

Experimental Details

Protonic micro devices are fabricated on p-type Si (Addison Engineering, B-doped, ρ = 0.001 ohm cm^{-1}) with thermally grown silicon oxide (100 nm). Standard photolithography is used to define the metal contacts. Pd (thickness from 1nm to 30 nm) with a 15 nm Cr adhesion layer is deposited via e-beam evaporation. To ensure consistency, contacts are kept at a 100 nm total thickness by adding Au between the Cr and Pd layers as needed. SU-8 is used to confine the Nafion covered area. 2 μL of Nafion 117 solution (5% concentration) from Sigma Aldrich is drop-cast on top of the patterned silicon wafer and the solution is dried in a fume hood. For protonic sandwich devices, Pd (50 nm) is evaporated on glass slides with 5 mm contacts defined by shadow masking with tape. A porous cellulose membrane (VWR Tissue Wipe) immersed in the Nafion solution is sandwiched between the two Pd contacts. The cellulose membrane prevents short circuit and improves the connection. Measurements are performed with a semiconductor parameter analyzer (Agilent 4155C). A Rigol DG4062 function generator is used to create a pulse sequence and sinusoidal inputs. Device testing is performed on a Signatone H-100 probe station in a controlled atmosphere of 5% H_2, 95% N_2, at 75% relative humidity (RH). In 5% H_2 atmosphere, Pd absorbs H_2 to form PdH_x (x=0.6) (*15, 22, 40, 41*). A finite difference model implemented in Matlab is used to calculate the diffusive flow of H within the contact. The simulated contacts are 30 μm wide by 10 nm thick, and are partitioned in 10 nm segments along a total contact length of 60 μm. D_H = 4 x 10^{-11} m^2 s^{-1} (*45*). Simulations are performed by repeating a two-step algorithm. First, the momentary inter-cell fluxes are computed based on the existing concentration in each cell. Second, the time is incremented by 1 μs, and new cell concentrations are computed from the given fluxes and conservation of mass.

3.2 Protonic Field Effect Transistors

Reproduced with permission from Nature Communications

As described in section 1.1, proton (H^+) conduction plays a key role in nature (*50*). Examples are oxidative phosphorylation of ATP for biological energy conversion in mitochondria (*51, 52*), the light activated proton pumping of bacteriorhodopsin in Archaea (*53*), proton activated bioluminescence in dinoflagellates (*54*), proton activated flagella in bacteria (*55*), the HVCN1 voltage gated proton channel in mammals (*56*), and the antibiotic Gramicidin (*57*). All of these systems use the Grotthus mechanism (*58*) of proton conduction decribed in section 2.1 (*59, 60*). These proton wires also support the transport of a proton vacancy, or proton hole, as OH^- (*61*). Discriminating between H^+ and OH^- transport with electrophysiological measurements is difficult because H^+ and OH^- have the same Nernst potential (*62*).

In this work, I build on the exciting demonstration of a proton conducting field effect transistor (H^+-FETs) as described by C. Zhong et. al. (*15*). Here I report proton-conducting devices with polysaccharide supported proton wires that are designed to preferentially conduct either H^+ or OH^-, as proton holes. The conductivity in these devices follows a model for proton semiconductivity proposed in 1958 by Eigen and de Maeyer (*17*). I demonstrate a H^+ - OH^- rectifying junction and H^+-type and OH^--type complementary FETs. With gate control of the current, these FETs unequivocally discriminate between H^+ and OH^- conductivity and confirm that proton wires support the conduction of OH^- as a proton hole.

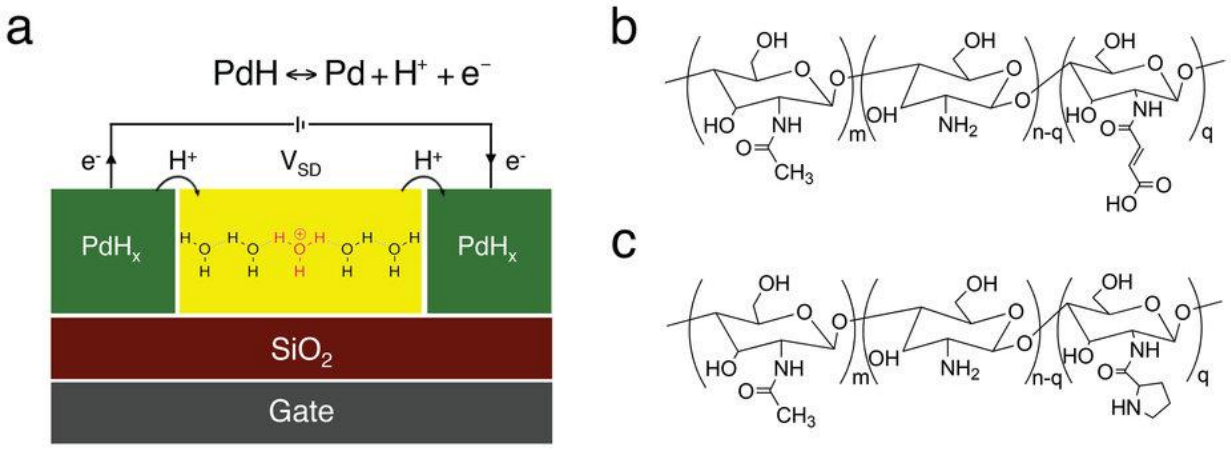

Figure 3.2.1. Complementary protonic biopolymers. (a) PdH_s contacts in an FET configuration. The gate electrode is used to electrostatically modulate the charge carrier density in the channel. (b) Molecular structure of the H^+-type proton conductor maleic chitosan. (b) Molecular structure of the OH^--type proton conductor proline chitosan. The degree of substitution, defined as q/n + m, determines the doping level.

Device Architecture and Materials.

This experiment used standard PdH_x contacts in an FET configuration (Fig. 3.2.1a). As described in section 2.3, PdH_x contacts will inject and drain protons into and from the proton-conducting channel, effectively serving as protodes (*15, 22, 40*). The contacts and the proton-conducting channel are insulated from the back gate by a SiO_2 (100 nm) dielectric layer. The proton-conducting channel is either maleic-chitosan (poly (*β* - (1,4)-*N-Maleoyl-D-glucosamine*)) (Fig. 1b) or proline-chitosan (poly (*β* - (1,4)-N-*proline-D-glucosamine*)) (Fig. 3.2.1c). These biopolymers are both derived from chitin and are of particular interest for developing future devices for bioelectronic applications. The synthesis of these materials was performed by

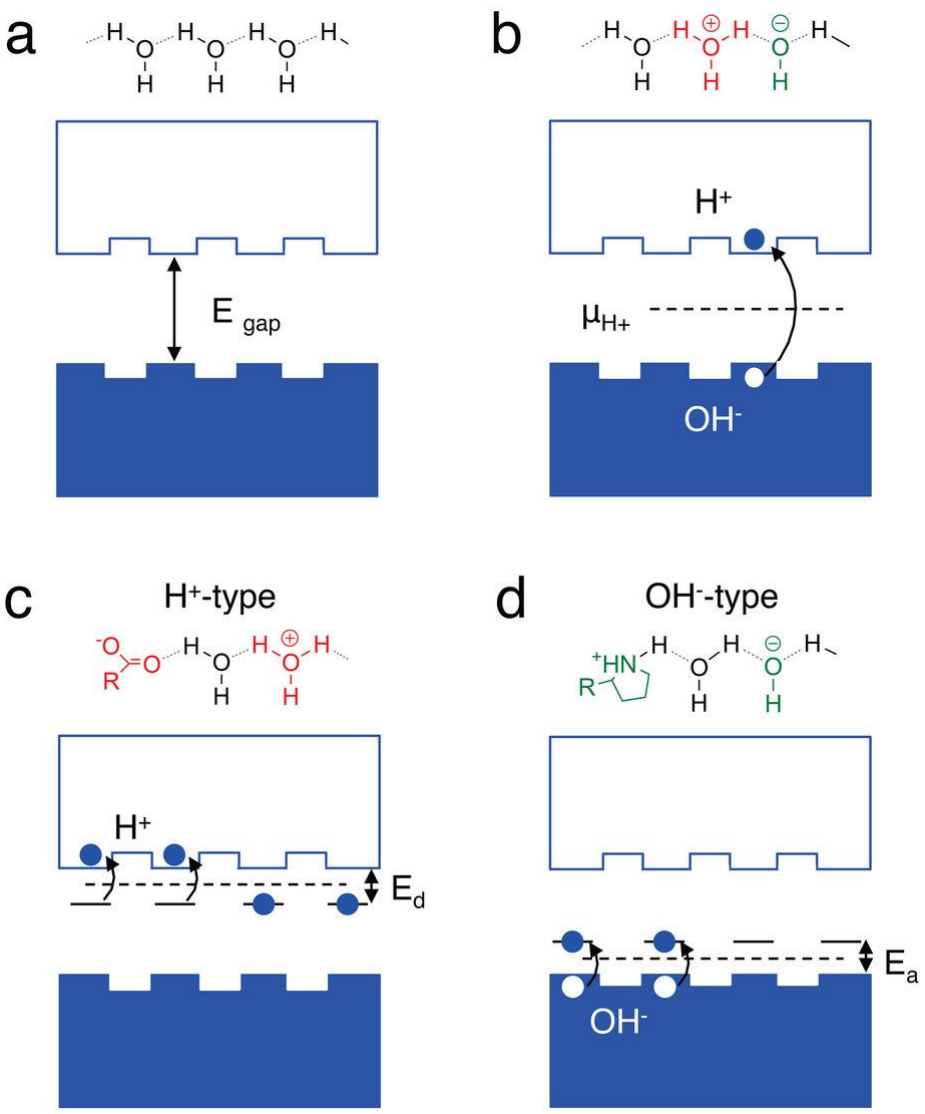

Figure 3.2.2 Band structure of protonic biopolymers. (a) A wire with no H^+ or OH^- defect does not conduct. The band gap is defined as the energy required to create a H^+OH^-pair (proton-proton hole) and is derived from the $E_{gap} = \Delta G^{0\prime} = -k_B T \ ln \ K_w$ = 0.83 eV (the Gibbs-Helmholtz equation). (b) For an intrinsic proton wire, the protochemical potential u_{H+} is in the middle of the band-gap. The H^+ is not completely delocalized along the conduction quasi band. Hopping barriers of approximately 100 meV need to be overcome for conduction to occur. (c) An acid donates a H^+ into the

conduction band of a proton wire to yield a H^+-type protonic conductor. $E_d = \Delta G^0_a = -k_B T \ln K_a$, K_a is the acid dissociation constant. The maleic acid group pK_a (-log K_a) = 3.2, which corresponds to E_d = 0.18 eV. (d) A base accepts a H^+ to create a OH^- (proton hole) in the valence band of a proton wire to yield a OH^--type protonic conductor. $E_a = \Delta G^0_b = -k_B T \ln K_b$, K_b is the base dissociation constant. The proline base pk_b (-log K_b = 3.4), which corresponds to E_a = 0.20 eV. For both H^+ type and OH^- type the protochemical potential is $\mu_C^{H+} = eV_0 + \mu_0 + k_B T \ln a_{H+}$ where a_{H+} is the activity of H^+.

Yingxin Deng. Chitin and most of its derivatives are biodegradable, nontoxic, and physiologically inert and are used in bionanotechnologies (*63-65*). Maleic-chitosan and proline-chitosan include several hydrophilic groups that participate in hydrogen bonding with water condensed from a humid atmosphere (20% *w/w* MC and 15% *w/w* PC at 75% RH) (SI). The resulting chains of hydrogen bonds form proton wires (*19, 52, 59*) along which protons hop according to the Grotthuss mechanism, as described in section 2.2.

A Model for Proton (H^+) and proton hole (OH^-) conductivity.

In 1958, Eigen and de Maeyer proposed a phenomenological description of proton conductivity in ice analogous to electron conductivity in a semiconductor (*17*). Ice is a water hydrogen bonded system that is made of proton wires similarly to protein membranes and the hydrated biopolymers used in this work.(*17, 19, 52, 59*) A proton wire without any H^+ or OH^- charged defects does not conduct unless an excess charge is injected from the contacts (Fig. 3.2.2a). The charge carriers (protons) are distributed between a “valence band” (H-bonded H_2O) and a

"conduction band" (excess protons fluctuating in hydrogen bonds). Protons are not delocalized along the proton conduction band, but are separated by potential barriers (Fig. 3.2.2a). These barriers represent the potential barrier for the proton to transfer from one molecule to the next. The height depends on the precise molecular structure, and is typically of the order of 100 meV. I define the protonic "band gap" as the energy required to create a H^+ (proton) and OH^- (proton hole) pair in the proton wire (Fig. 3.2.2b). I derive this energy from the Gibbs Helmholtz equation and the dissociation constant of water (K_w) as

$$E_{gap} = \Delta G^0 = -k_B T \ln K_w = 0.83 \text{ eV}. \qquad (3.2.1)$$

This value for the protonic "band gap" is similar to the activation energy measured for proton conducting biopolymers (*20, 21*), and remarkably close to the band gap of traditional electronic semiconductors such as Si (1.1 eV) or Ge (0.76 eV). Not unlike Si and Ge, the conductivity of most intrinsic biological protonic conductors at room temperature is low (*66*).

To increase the conductivity of the proton wire, doping is used to introduce H^+ and OH^- (proton hole) charge carriers. An acidic functionality in the hydrogen bond network (Fig. 3.2.2c) donates an H^+ to the proton wire "conduction band" in the same way a group V (P, As) impurity donates an electron in the Si conduction band. I derive the position of the H^+ donor state respect to the "conduction band" by substituting K_w with K_a (acid dissociation constant) in eq. 3.2.1. For maleic-chitosan (pK_a 3.2), E_d= 0.18 eV. A basic functionality in the hydrogen bond network (Fig. 2d) accepts a H^+ to create an OH^- proton hole in the proton "valence band" in the same way a group III (B) impurity creates a hole in the Si valence band. For proline-chitosan I use pK_b= 3.4 in (Eq. 3.2.1) to calculate E_a= 0.2 eV. The position of the protochemical potential is calculated from

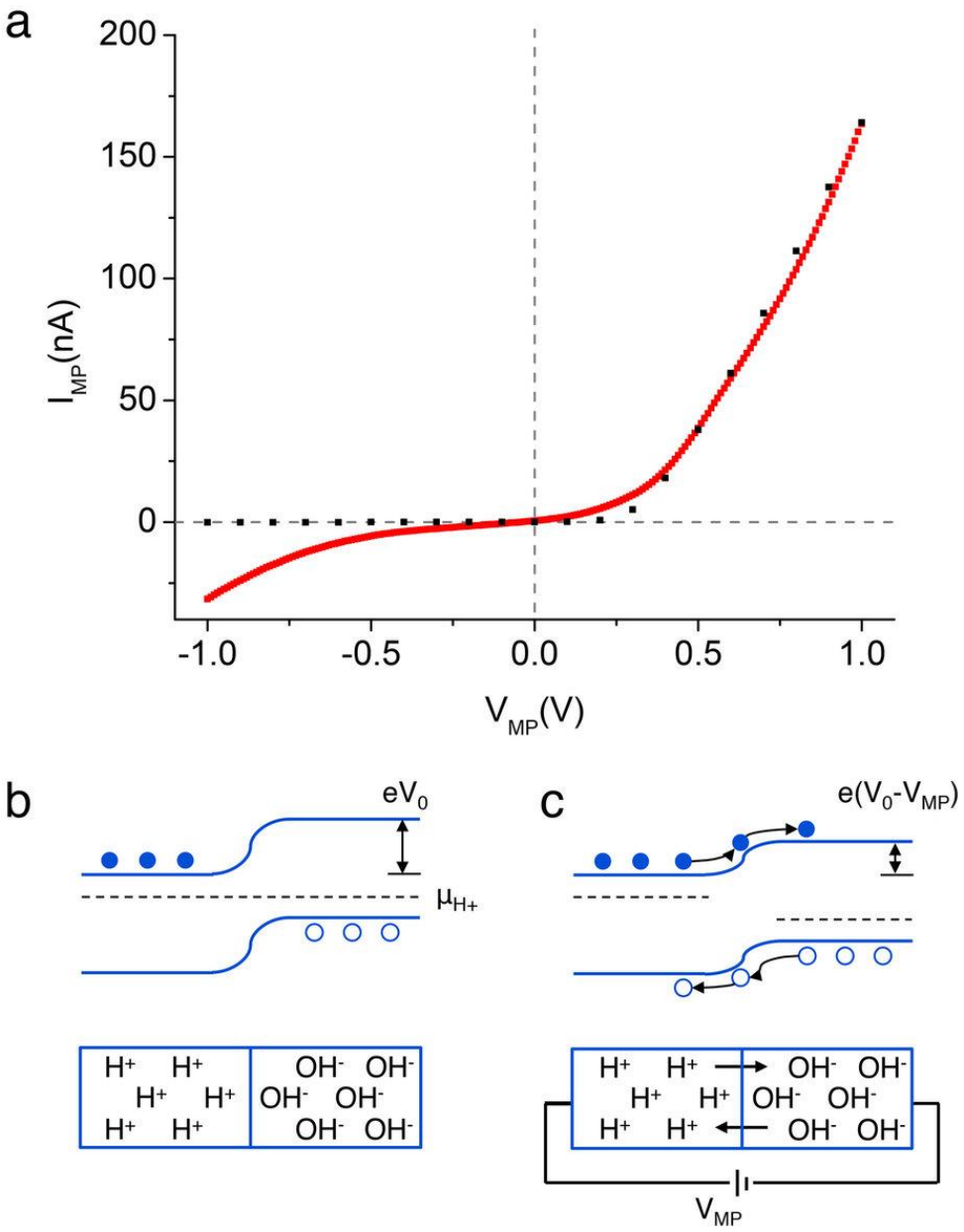

Figure 3.2.3 A protonic pn junction. (a) Red trace- Experimental data for IV characteristics of a H^+ - OH^- junction formed by maleic chitosan and proline chitosan. The curve shows the expected nonlinearity. Black dots - data from simulations for the same junction using the semiconductor model. (b) When H^+ doped and OH^- doped material are placed into contact, OH^- diffuse into the H^+ region and H^+ diffuse into the

OH^- region until the μ_{H+} on both sides is the same. H^+ and OH^- recombine in the depletion region. A contact potential V_0 occurs across the junction and is dependent of the difference in μ_{H+} of both sides. (c) A forward bias (V_{MP}) applied between source and drain reduces the contact barrier by $e(V_0-V_{MP})$ and induces thermionic emission of H^+ into OH^- side.

the activity of H^+, or the pH, and Nernst equation as $\mu_C^{H+} = eV_0 + \mu_0 + k_BT \ln a_{H+}$ (a_{H+}= activity of H^+). (60) Qualitatively, μ^{H+} in a protonic semiconductor is affected by doping the same way the Fermi energy in an electronic semiconductor is affected. For an intrinsic material, μ^{H+} is at mid gap. For H^+-type material, μ^{H+} is closer to the conduction band and for an OH^- - type material μ^{H+} is closer to the valence band. The intrinsic version of maleic chitosan and proline chitosan is unmodified chitin. Chitin does not have functional groups that contribute H+ or OH^- dopants to the proton wires. As expected, the protonic conductivity of chitin measured with PdH_x contacts is significantly smaller than the protonic conductivity of maleic chitosan or proline chitosan.

A H^+-type and OH^--type Junction.

As part of their model that compares H^+-type and OH^--type protonic semiconductors with electronic semiconductors, Eigen and de Mayer propose a H^+ - OH^- junction in ice with acid and base dopants (*17*). Similarly, here I measure the properties of maleic-chitosan (H^+-type) and proline-chitosan (OH^--type) junction devices with proton conducting contacts under 75% RH (Fig. 3.2.3). When a potential difference between the contacts is applied (V_{MP}), the measured current (I_{MP}) shows asymmetric characteristics as expected (Fig. 3.2.3a). The dependence of I_{MP}

on V_{MP} in the H^+ -OH^- junction is easily described with the semiconductor model (Fig. 3.23b &c). At first contact, the gradient in μ^{H+} drives the diffusion of H^+ into the proline-chitosan and OH^- into the maleic-chitosan until equilibrium is reached. The charge carriers recombine at the junction as H_2O and create a depletion region with an associated contact potential (V_0) (Fig. 3.2.3a). This H_2O generated at the interface does not affect the hydration of the polymers at the interface because the overall concentration of recombined H^+ and OH^- is negligible compared to the water already present in the biopolymers. A positive potential on the H^+-type side (forward bias) reduces V_0 and results in a net thermally activated current of H^+ and OH^- across the forward biased junction (Fig. 3c). At the same time, a negative potential on the H^+-type side increases the potential barrier and results in very little current going across the reverse biased junction. This model is used to simulate the junction characteristics (Fig. 3.2.3a). I treat the maleic-chitosan and the proline-chitosan as n-type and p-type electronic semiconductors (switching the sign of the charge carriers) with a band gap of 0.8 eV. The doping concentration is calculated using the semiconductor model (Fig. 3.2.2 c & d). The number of H^+ donated by the maleic-groups in the proton "conduction band" is calculated from the maleic acid pK_a and the density of the maleic group on the chitosan backbone (Fig 3.2.1b). In turn, the number of OH^- proton holes created by the proline-base in the proton "valence band" is calculated from the proline base pK_b and the density of proline groups on the chitosan back bone (Fig.3.2.1c). For maleic-chitosan, I obtain $n^{H^+}_{maleic}$ = 8.9 x 10^{17} cm^{-3} and for proline-chitosan $n^{OH^-}_{proline}$ = 4.3 x 10^{17} cm^{-3}. The contribution to the charge carrier doping of the unreacted $-NH_2$ in chitosan (Fig. 3.2.1 b & c) can be neglected. The dissociation constant of these amines (pk_b= 7.5) is low and results in OH^- doping at least two orders of magnitude lower than the

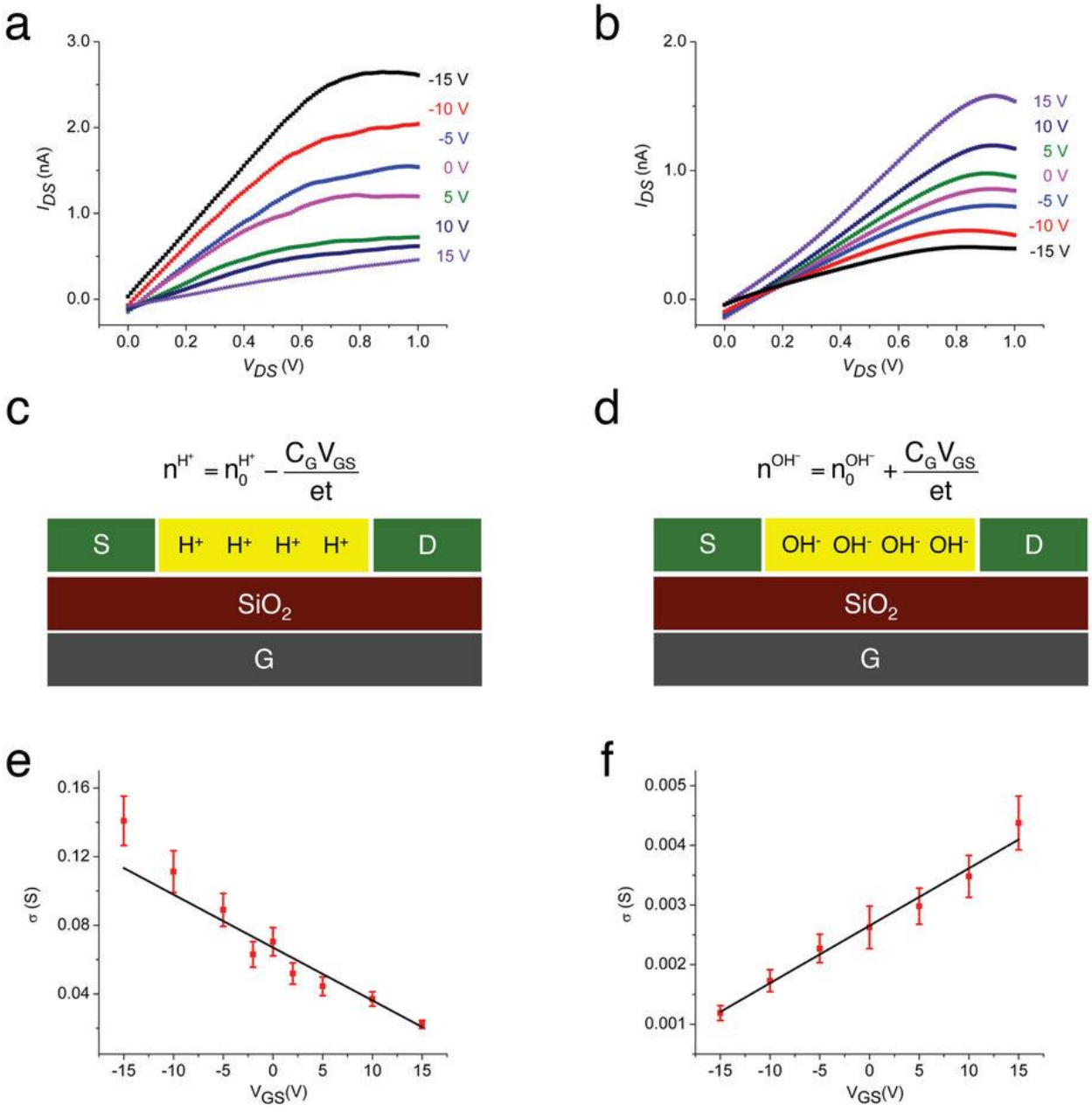

Figure 3.2.4. Complementary protonic devices. (a) (b) Plots of I_{DS} as a function of V_{GS} for different V_{DS} (RH 75%) for a maleic chitosan H^+-FET and a proline chitosan OH^--FET with PdH_x contacts. Device dimensions: length 8.6 µm, width 3.5 µm, height 82 nm for (a) and 9.6 µm, width 28 µm, height 200 nm for (b). The small deviation of I_{DS} from zero at V_{DS} = 0 is likely due to hysteresis as previously observed for these

types of devices, (c) (d) Schematics of H^+ and OH^- transistor capacitative charge carrier n^{H+} and n^{OH-} modulation. (c) $n^{H^+} = n_0^{H^+} - \frac{C_G V_{GS}}{et}$ (C_G = gate capacitance per unit area, t = device thickness) (d) $n^{OH^-} = n_0^{OH^-} + \frac{C_G V_{GS}}{et}$. From simulations of dQ/dV_{gs}, C_g = 3.85 × 10^{-4} F m^{-2}. (e) (f) Plots of $\frac{\partial J_{DS}}{\partial \varepsilon_{DS}} = \sigma$ as function of V_{GS} and linear fit for the device in (a) and (b) respectively. For cross σ and charge density calculations the cross sectional area of the devices was derived from AFM and the cross sections were approximated to a rectangle with t = 66 nm for (a) and t = 160 nm (b) with the same widths as the actual devices. From the fi, $\mu_{lin} = \pm \frac{t}{C_G} \frac{\partial \sigma}{\partial V_{GS}}$ and $n_0 = \frac{\sigma|_{V_{GS}=0}}{e\mu_{lin}}$.

doping from the proline or the maleic groups. The mobility data for the charge carriers is derived from the H^+-FET and OH^--FET devices (Fig. 3.2.4). In the forward bias region, the overall shape of the curve matches the shape of the experimental data well for a minority carrier recombination time of 1 μ s. This recombination time is remarkably close to the recombination time of H^+/ OH^- in neutral water (35 μ s) (*17*) and appropriately smaller because of higher H^+/ OH^- concentration in the devices. Despite the applied voltages being below electrolysis levels, the increased back bias current may be due to field-induced water splitting at the contacts as previously observed in bipolar ion-exchange membranes (*67*). To appropriately simulate the experimental conditions, I scale the current in a 1x1 μ m^2 junction by several fold, but not by the exact amount required to recreate exactly a junction with 1x1 cm^2 contacts. The H^+-type OH^--type junction is assembled from pre-formed components and results in a device with

overall poor physical contact. This poor physical contact effectively reduces the area of the junction and the area of the contacts. Despite these shortcomings, the junction devices show the expected rectifying behaviour, which is qualitatively matched by the simulations.

Complementary Bioprotonic Field Effect Transistors.

To confirm the proton semiconductor model, I analyse the output characteristics of complementary protonic-FET devices. In a protonic-FET type device (Fig. 3.2.1a), the source-drain protonic current, I_{ds}, recorded as a function of drain-source bias, $V_{DS,}$ is controlled by changing the potential of the back gate electrode, V_{GS}. As previously reported(*15*), for the maleic-chitosan H^+-FET (Fig 3.2.4a), a negative V_{GS} results in a higher source-drain current for the same V_{DS}, while a positive V_{GS} almost turns I_{DS} off. This V_{GS} dependence of I_{DS} is consistent with an FET with positive charge carriers (H^+). This type of electric field modulation of H^+ has also been demonstrated in Nafion based field-effect devices (*68*). In turn, the proline-chitosan OH^--FET shows the opposite V_{GS} dependence. A negative V_{GS} almost turns the device off and a positive V_{GS} results in higher I_{ds} (Fig. 3.2.4b). This V_{GS} dependence of I_{DS} is consistent with an FET with negative charge carriers (OH^-). Both kind of devices show current saturation for higher V_{ds} and corresponding I_{DS}. Both kinds of devices show current saturation for higher V_{ds}. This saturation may be due to charge accumulation at the contacts and the formation of a barrier for higher I_{ds} as previously discussed (*15*). Further investigation of the contact barrier for the devices is required to confirm this hypothesis.

I explain the I_{ds} modulation from V_{GS} in these devices with the gradual channel approximation (*69*):

$$I_{DS} = \pm\mu_{lin} C_G \frac{W}{L}\left[(V_{GS} - V_{TH})V_{DS}\right] \qquad \text{(eq. 3.2.2)}$$

(+ for a negative charge carrier and – for a positive charge carrier, μ_{lin}=mobility in the linear regime, C_G= gate capacitance per unit area, W=device width, L= device length, V_{TH}=threshold gate voltage at which conduction occurs). A few modifications are required to eq. 3.2.2 to take into account that in the accumulation mode devices I cannot reach the V_{TH} at which the channel is completely depleted of charge carriers. I first rewrite eq. 2 as:

$$J_{DS} = \pm\mu_{lin} \frac{C_G}{t} V_{GS}\varepsilon_{DS} \qquad \text{(eq. 3.2.3)}$$

(J_{ds}= source drain current density, $C_{GS}V_{gs}/t$= charge carrier per unit volume induced by the gate, ε_{DS}= V_{DS}/L=electric field along the device channel) and compare it to:

$$J_{DS} = \sigma\varepsilon_{DS} = e\mu_{lin} n\varepsilon_{DS} \qquad \text{(eq. 3.2.4)}$$

(σ = channel conductivity, n=charge carriers per unit volume, e=elementary charge). I then modify n to take into account for the H^+ (n_0^{H+}) or OH^- (n_0^{OH-}) from acid and base doping already in the channel at V_{GS}=0. This modification results in:

$$n^{H+} = n_0^{H^+} - \frac{C_G V_{GS}}{et} \qquad \text{(eq. 3.2.5)}$$

or H^+-FET and

$$n^{OH^-} = n_0^{OH^-} + \frac{C_G V_{GS}}{et} \qquad \text{(eq. 3.2.6)}$$

for OH^--FET respectively (Fig. 3.2.4 c and Fig. 3.2.4d). For an intrinsic semiconductor, these modifications cannot be used by simply setting n_0=0. V_{TH}, in this case the voltage at which the Fermi energy of the intrinsic semiconductor is shifted enough to afford injection of charge carriers into one of the bands, should be included back in eq. 3.2.2. Using equation 3.2.5 and equation 3.2.6, equation 3.2.3 becomes:

$$J_{DS} = e\mu_{lin}^{H^+}\left(n_0^{H^+} - \frac{C_G V_{GS}}{et}\right)\varepsilon_{DS} \qquad \text{(eq. 3.2.7)}$$

for H^+-FET and:

$$J_{DS} = e\mu_{lin}^{OH^-}\left(n_0^{OH^-} + \frac{C_G V_{GS}}{et}\right)\varepsilon_{DS} \qquad \text{(eq. 3.2.8)}$$

for OH^- -FET. To calculate $\mu_{lin}^{H^+}, \mu_{lin}^{OH^-}, n_0^{H^+}$, and $n_0^{OH^-}$, I plot $\frac{\partial J_{DS}}{\partial \varepsilon_{DS}} = \sigma$ as a function of V_{GS} (Fig. 3.2.4 e and 3.2.4f). $\mu_{lin}^{H^+}, \mu_{lin}^{OH^-}$ are derived from the gradient of the linear fit and $n_0^{H^+}$ and $n_0^{OH^-}$ are derived from the intercept (Fig. 3.2.4 e and 3.2.4f)(*69*). From the devices, $\mu_{lin}^{H^+} = (5.3 \pm 0.5)10^{-3} cm^2 V^{-1} s^{-1}$ and $\mu_{lin}^{OH^-} = (0.40 \pm 0.02)10^{-3} cm^2 V^{-1} s^{-1}$. The mobility for H^+ is remarkably close to the mobility for H^+ in diluted acidic solutions (*58*) and in hydrated semiconducting polymers,(*70*) and is slightly higher than H^+ mobility of Nafion (0.87×10^{-3} cm^2 $V^{-1}s^{-1}$) proton exchange membranes widely used in fuel cells.(*71, 72*) Matching the H^+ mobility in water solutions is important for potential future biological applications where the H^+ are transferred in liquid. For basic solutions, the mobility of OH^- is lower than H^+ and reported as

1.96 x 10^{-3} cm^2 V^{-1} s^{-1}. The OH^--type devices show a mobility that is in reasonable agreement with this value, but is five-fold lower than expected. A few factors may contribute to the lower than expected OH^- mobility. The proline chitosan in the OH^- -FET contains less water (15% *w/w*) than the maleic-chitosan in the H^+-FET (20% *w/w*). This lower water content results in a smaller number of pathways, or proton wires, for the OH^- to conduct. Maleic chitosan forms self-assembled nanofibers while proline chitosan forms an amorphous film on the substrate (Fig. S5). The more ordered morphology of the maleic chitosan also likely contributes to the higher proton mobility in the H^+-FET respect to the OH^--FET. In this analysis, I have neglected the effects of the contacts. It is likely that the contact between the PdH_x and the proton-conducting channels is affected by the difference in protochemical potentials. From the data for the PdH_x reversible electrodes in acidic solutions(*73*), one infers qualitatively that the protochemical potential of the PdH_x is closer to the protochemical potential of the H^+-type maleic chitosan and is significantly higher than the protochemical potential of the OH^--type the proline chitosan. PdH_x is thus more likely to form a better protonic contact (Ohmic) with maleic-chitosan, while a potential barrier at the PdH_x- proline-chitosan contact may occur. This barrier is similar to a Schottky barrier that occurs between a metal with low work function and a p-type electronic semiconductor. This potential explanation, however, requires further investigation and will be addressed in future work. With the values of the mobility, I extrapolate $n_0^{H^+} = (8.0 \pm 0.4)10^{17} cm^{-3}$ and $n_0^{OH^-} = (4.0 \pm 0.1)10^{17} cm^{-3}$ for the devices. The values are compared with $n_{maleic}^{H^+}$ = 8.9 x 10^{17} cm^{-3} and $n_{proline}^{OH^-}$ = 4.3 x 10^{17} cm^{-3} derived from the acid and base doping semiconductor model (Fig. 3.2.2). Given all the assumptions made in deriving the values from the acid and base doping, the agreement is good. This agreement confirms that the

semiconductor doping model is an appropriate description for proton transport in doped proton wires measured with these devices. Further work is needed to generalize this model to intrinsic semiconductors to take into account the turn on voltage, V_{TH}. For this work, devices with higher gate capacitance capable of turning on the intrinsic devices at a reasonable V_{TH} are required.

Discussion

In summary, I have demonstrated H^+ -OH^- rectifying junctions and H^+- type and OH^- -type complementary field effect transistors with polysaccharide based biomimetic proton wires. These devices confirm that proton wires support the conductivity of OH^- as proton holes. I describe the conductivity in these devices with a model in which H^+ (protons) and OH^- (proton holes) are equivalent to electrons and holes in semiconductors. This model was originally proposed by Eigen and de Maeyer and refined to include band gap calculations and effects of doping on the protochemical potential. The mobility for H^+ and OH^- in the devices $\mu_{lin}^{H^+} = (5.3 \pm 0.5)10^{-3} cm^2 V^{-1} s^{-1}$ and $\mu_{lin}^{OH^-} = (0.40 \pm 0.02)10^{-3} cm^2 V^{-1} s^{-1}$, are in good and reasonable agreement with what has been previously reported for the same species in other hydrogen-bonded systems. The on-off ratio of these devices is low (~ 3-4), but closely agrees with electrostatic modelling. Avenues for improvement include using thinner gate dielectrics and high k gate dielectrics. The field effect manipulation of H^+ and OH^- currents may be used, in the future, to interface with proton conducting ion channels (*6*). However, for these applications devices that function in physiological conditions need to be developed, given that the current devices are extremely sensitive to the water content in the polysaccharides. The H^+ and OH^-

mobility in the devices is comparable to the mobility of ions in solution, therefore the performance of these polysaccharides does not limit the potential coupling with biological systems. The ability to precisely control the flow and concentration of H^+ and OH^- may also be used to study the kinetics of acid-base chemical reactions (*52*). Finally, given the importance of protonic conduction in biological energy conversion and electrophysiology in general, insights from the semiconductor model and protonic devices may prove useful at interrogating the conductivity in relevant proton channels from an alternate perspective.

3.3 Proton Transfer Between PdH_x and Solution

The pH of a hydrated polymer is analogous to the pH of an aqueous solution. Therefore, with the assistance of Takeo Miyake I have conducted electrochemical measurements to measure the behavior of the PdH_x-solution interface and ensure that the PdH_x-solution interface does not limit proton flow (*74*).

In this experiment, Pd contacts are immersed in a buffered solution of known pH. Electrical measurements are conducted in a three-electrode configuration, with an Ag/AgCl reference electrode (Figure 15). In an electrochemical measurement, no current is allowed to flow through the reference electrode(*75*). Therefore, the solution potential is equal to the reference potential, plus an offset due to their differing work functions. Measurements are conducted with the counter and working electrode in feedback. The counter electrode current is varied to control the potential difference between the reference and working electrodes. The resulting equilibrium reveals the current flow across the interface for a specified potential difference.

Measurements showed the familiar dissociation reaction $PdH \rightarrow Pd + H^+ + e^-$ for small positive voltages. In addition, negative voltages cause the reverse reaction $Pd + H^+ + e^- \rightarrow PdH$. This allows the formation of PdH from solution without any H_2 gas, which is beneficial since H_2 gas is corrosive for many materials. The voltage required for either process depends on the pH of the solution. For some voltages, the reaction does not proceed in either direction. This 'dead-zone' is useful for long-term storage of H within Pd.

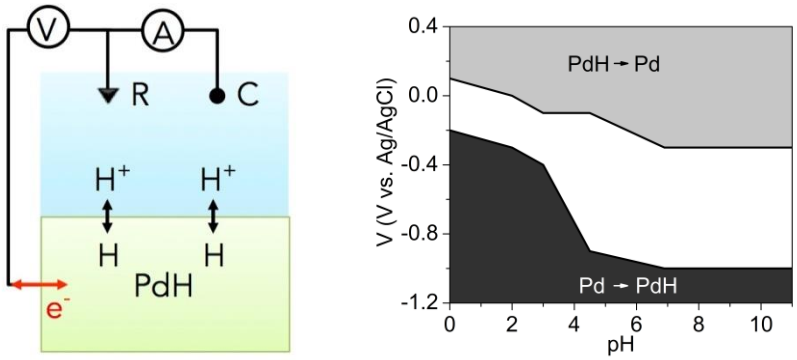

Figure 3.3.1. Electrochemical PdH Formation. Left: schematic of electrochemical measurements. The flow of protons into or out of the PdH is governed by the solution potential as set by the reference and counter electrodes. Right: formation and depletion conditions for PdH. The voltage required depends on the pH of the solution. A significant dead-zone indicated in white allows stable storage of hydrogen for long periods (*74*).

3.4 The Palladium-Nafion Interface

My experiments on Nafion and biomaterials suggest that these materials are strongly impacted by interface effects at the boundary with the palladium hydride contact. If unaccounted for, non-linear interface effects related to the injection of protons from the PdH_x contact into the channel can obscure conductivity measurements and interfere with device behavior. To understand these interface effects, they must be isolated from any channel behaviors. In addition, a precisely defined contact surface area is required to establish the current density and ensure a uniform interface potential. Understanding the proton injection dynamics will allow more precise measurements in future work, and allow the tailoring of device geometry to match specific experimental needs.

Experiment

I fabricated a micro-scale four point probe device to make more precise measurements of the interface behavior (Fig 3.4.1 A). This system includes two Au contacts in the channel, to separate bulk and interface behaviors. In the language of traditional electrochemistry, the source is the working electrode, the drain is the counter electrode, and the two Au probes are a reference electrode that corrects for the resistance of the electrolyte. To control the contact surface area, I added an SU-8 layer to limit the channel width and interface area. I fabricated these devices with standard contact lithography on Si wafers capped with a 100nm SiO_2 layer. 100nm thick, 40um wide Pd contacts were deposited with separations of 20, 50, 100, and 200µm using electron beam evaporation. 50nm thick, 3um wide Au contacts were then deposited within this channel, with a Pd edge to Au center distance ($L_{Pd\text{-}Au}$) of 5.5um for all

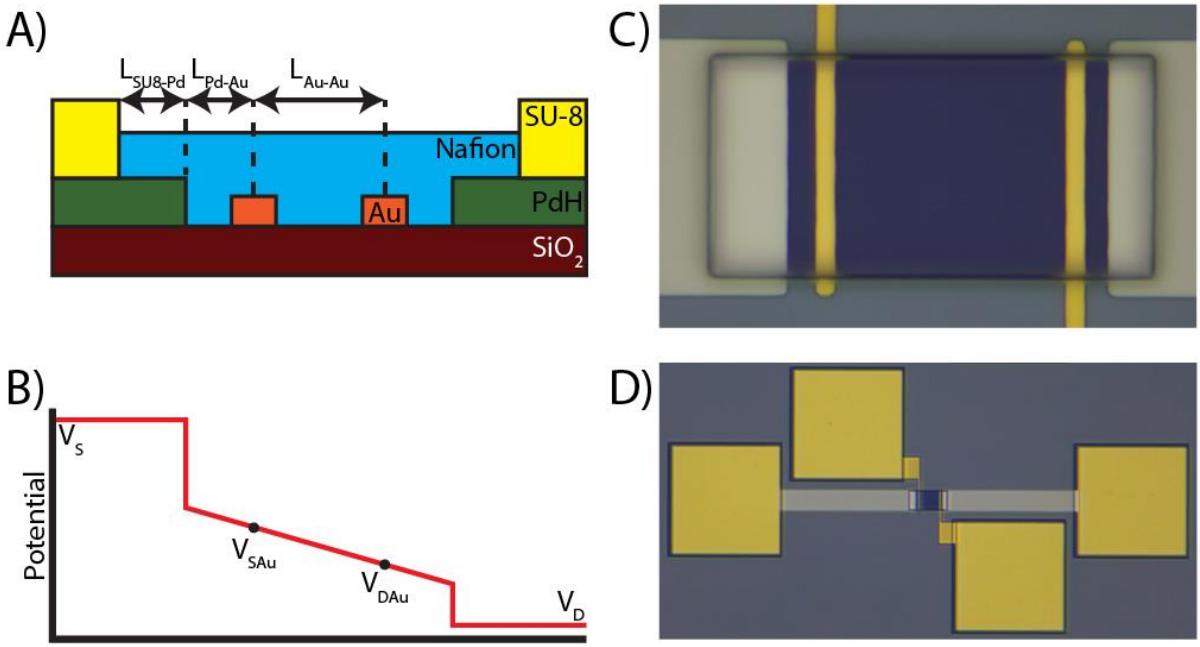

Figure 3.4.1. Four Point Probe Device Geometry. A) Cross section of the micro-scale four point probe device. B) Electric potential within the four point probe device. The slope of the $V_{SAu} - V_{DAu}$ line is proportional to the conductivity of the bulk material. The interface voltage at the source (V_{SInt}) and drain (V_{DInt}) is calculated by a simple linear extension of this slope, using the geometric parameters from A). C) Top-view image of the fabricated device before Nafion deposition. This image was composited from three images at different focal planes. D) Layout of the contact pads and device connections in a 50µm device. From left to right, pads are for V_S, V_{SAu}, V_{DAu}, and V_D.

lengths. A 5nm Cr layer beneath both Pd and Au layers keeps the metals adhered to the SiO_2 surface. Next, I patterned a 4µm thick SU8 channel on top of the metal layers. The SU-8 channel exposes a 10µm deep, 35µm wide area of Pd at each end of the device, for a total exposed area of 350 μm^2 at both source and drain contacts (Figure 3.4.1 C). The layout of the device, including contact pads, is shown in Figure 3.4.1 D. Just before each measurement, I

used spin-coating to deposit a uniform 300nm layer of Nafion from solution, then baked the device at 80C for 5 minutes to remove any residual solvents.

During the measurement, I apply a voltage to the source (V_S) and drain (V_D), then measure the current (I_S). In addition, I hold both Au probes in feedback at zero current, then measure the resulting voltage near the source (V_{SAu}) and drain (V_{DAu}). The potential profile of the device is shown in Figure 3.4.1 B, and an example of the measured data in Figure 3.4.2 A. Assuming that the potential drop in the channel is linear, I calculate the voltage drop at the source-channel interface to be:

$$V_{SInt} = V_S - V_{SAu} - (V_{SAu} - V_{DAu}) * \frac{L_{Pd-Au}}{L_{Au-Au}} \qquad \text{(eq 3.4.1)}$$

and the voltage drop at the channel-drain interface to be:

$$V_{DInt} = V_{DAu} - (V_{SAu} - V_{DAu}) * \frac{L_{Pd-Au}}{L_{Au-Au}} - V_D \qquad \text{(eq 3.4.2)}$$

Here, $L_{Au\text{-}Au}$ is the center to center distance between the two Au electrodes.

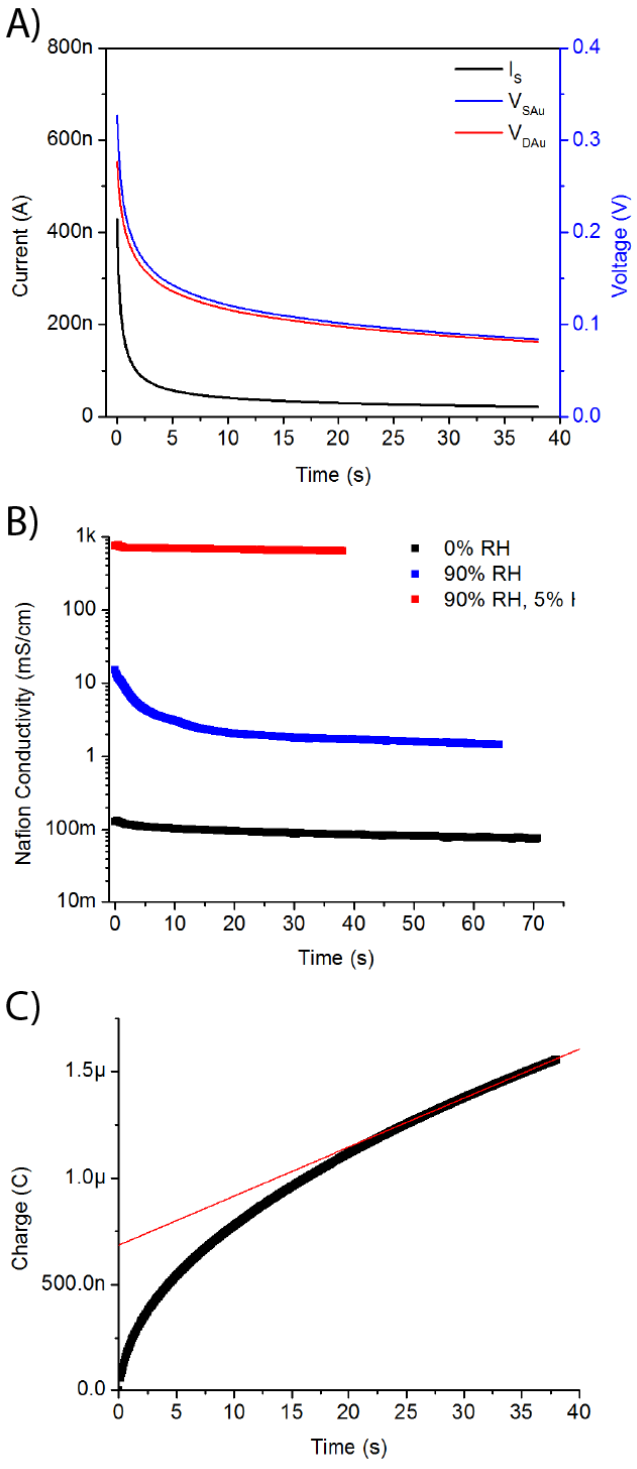

Figure 3.4.2. A) Unprocessed results from the four point probe measurement at 90% RH and 5% H_2. The current, voltages, and voltage difference all decay exponentially. B) Nafion conductivity vs. atmospheric conditions. As expected, the proton conductivity

(red) is higher than the ion conductivity (blue) and electron conductivity (black). The decay in ionic conductivity suggests the slow formation of a Debye layer. C) Total charge transferred through the device vs. time. The charge increases continually with time, indicating that the absorption rate of hydrogen gas from the atmosphere is significant.

I assume that I_S is the same for all calculations, since there should be very little leakage current into the Au electrodes or SiO_2 substrate. Therefore, the device current is uniform, and the current into the drain is equal to the current out of the source. The bulk material conductivity can be calculated as:

$$\sigma_{Nafion} = \frac{I_S L_{Au-Au}}{(V_{SAu} - V_{DAu})wt} \qquad \text{(eq 3.4.3)}$$

Here, w is the channel width (35um) and t the thickness of the Nafion layer (300nm).

The derived conductivity (Figure 3.4.2 B) depends strongly on the atmospheric conditions of the sample, as expected for the palladium hydride system (section 2.3). When dry (0% RH, black) the sample conducts electrons at a rate of only 0.13mS/cm. When hydrated (90% RH, blue), the conductivity initially increases to 15mS/cm, but gradually decays to 1.4mS/cm over the duration of the measurement. This decay is characteristically consistent with the formation of a Debye layer from ionic motion in the Nafion layer. Finally, the addition of hydrogen (90% RH, 5% H2, red) increases the derived conductivity to 730 mS/cm. As expected, this conductivity is constant over time despite the rapid exponential decrease in proton current during the measurement due to depletion (Fig 3.4.1 C, black). However, this derived conductivity is not consistent with the accepted literature conductivity of 78mS/cm (*43*).

Several effects may be responsible for this inconsistency. First, the Nafion layer thickness may swell by as much as 70% when fully hydrated (*76*). However, all thickness measurements were made on dry samples. Secondly, the measured voltage difference between the Au probes is very small, and therefore sensitive to even minor fluctuations. Typical channel voltages are around 50mV, while interface voltages are around 600mV (source) and 350mV (drain) (table 3.4.1). A 5% error in the source interface voltage gives a variation of ± 30mV, and if this error is inaccurately attributed to the channel the resulting error in conductivity is around 250%. Therefore, small errors or effects in the interface measurement can introduce large errors in the channel voltage.

Length	V_{SAu}	V_{DAu}	V_{Au-Au}
20um	334mV	250mV	84mV
50um	355mV	305mV	50mV
100um	367mV	299mV	68mV
200um	376mV	302mV	74mV

Table 3.4.1. Channel voltage length dependence. For ohmic conduction, the voltage across a material (V_{Au-Au}) should increase linearly with length. The observed behavior is instead noisy and non-linear, demonstrating that ohmic conduction has a minimal effect on the device behavior.

Critically, the measured voltage drop is not proportional to the device length, although it should vary linearly (Table 3.4.1). This confirms that the observed behavior is not ohmic in origin, and the derived conductivity is incorrect. The most likely source of error in this measurement is the presence of sidewall connections across the SU-8 steps in the device. Using the literature conductivity of 78mS/cm for Nafion, the expected resistance of a 300nm Nafion layer in the SU-8 trench that forms the channel is 1.2 MΩ. However, a 300nm thick Nafion layer is also deposited on top of the SU-8 during spin-coating. The rectangular area of Nafion between the

source and drain pads (Figure 3.4.1 D) has a resistance of around 2MΩ. In an ideal device, no Nafion would be deposited on the sides of the SU-8, so this layer would make no contact to the contact pads and therefore not affect the device. However, even a 3nm layer of Nafion deposited on the SU-8 walls would connect the contact pads to the top layer with a resistance of only 0.9MΩ. Therefore, conduction through the sheet of Nafion between the source and drain contact pads could occur with a resistance as low as 3.8MΩ, significantly affecting the 1.2MΩ expected resistance. Further, the close proximity of the contact and channel pads means that the resistance between these pads is even lower than 3.8MΩ. As discussed previously, the measured channel voltage difference is small, so even a high-resistance connection between e.g. V_S and V_{SAu} could have a significant effect on the derived conductivity. Unfortunately, the sidewall thickness is not known, so it is difficult to calculate how this connection affects the device behavior.

Charge

For further insight into the device dynamics, I calculate the total charge conducted through the device by integrating I_S against time (Fig 3.4.2 C). The charge transfer exponentially approaches a line. The slope of this line represents the equilibrium rate of current flow, which is inherently limited by the absorption of hydrogen gas from the atmosphere. Assuming that the absorption rate is constant with time, any other charge conducted must have been stored in the device before the measurement began. Therefore, the intercept of the line represents the total amount of H stored in the device. The derived initial charge from this intercept is 680nC.

A PdH_x contact with a 5% partial pressure of hydrogen will equilibrate at x ≈ 0.6 (Fig 2.3.2, (*23*)). Therefore, the total charge of protons stored as hydrogen in a contact is given by:

$$Q = \frac{Vqx\rho_{Pd}}{m_{Pd}} \qquad \text{(eq 3.4.4)}$$

Here, V is the contact volume, ρ_{Pd} the density of palladium, m_{Pd} the atomic mass of palladium, and q is the fundamental charge. The contacts used in this measurement have a volume of 35µm x 10µm x 100nm, so at x = 0.6 they will hold 230nC of charge. Therefore, 450nC of charge is unaccounted for. This amount of hydrogen could not be stored in the Nafion layer, as the solubility of hydrogen in Nafion is 0.01 mol/dm^3 (*77*), and the relevant Nafion volume is that just above the contact with total volume of 35µm x 10µm x 300nm. Therefore, the Nafion can contain ≈1 femtomole of hydrogen atoms, equal to only 100pC. Separately, it is possible that some hydrogen exists as an adsorbed layer on the Pd surface. The evaporation process results in a rough poly-crystalline surface, which may have a larger than expected surface area.

In electrolyte solutions, significant charge can be stored in a Debye layer. In addition, a long charged layer adjacent to the Pd contact might influence the Au probes and explain the Pd-Au correlation found in the bulk conductivity measurement. The Debye layer thickness is given by:

$$\lambda_D = \sqrt{\frac{\varepsilon D}{2\sigma}} \qquad \text{(eq 3.4.5)}$$

Here ε is the permittivity, D is the diffusion constant, and σ is the conductivity of the electrolyte material. Estimating that ε = 20 ε_0, D = 10^{-4} cm^2/s (*78*), and σ = 78mS/cm (*43*), I find λ_D = 0.33nm. This estimate assumes that the Nafion is very highly hydrated, with a water volume fraction of 1. Since the Pd to Au minimum distance is 4µm, it is unlikely that the 0.33nm Debye

layer at the Pd source has any influence on the Au contacts. From this estimate I can also estimate the capacitance of the layer, as:

$$C = \frac{\varepsilon A}{\lambda_D} \qquad \text{(eq 3.4.6)}$$

Here A is the area of the charge source interface (10um x 35um). This gives a capacitance of C = 188pF. For an applied V_S = 1V, the total charge is then Q = CV = 188pC. This is nominal compared to the 680nC initial charge in the device, so the Debye layer is unlikely to have any significant effects on the device. Similarly, capacitance at the large contact pads may be significant. There are 4 pads, of size 200µm by 200µm. The capacitance from the pads through the 100nm SiO_2 surface to the silicon substrate is small, at 0.15nF. However, the contact pads are coated with Nafion from the spin-coating process, and the Debye layer capacitance at these pads is significant. Using eq 3.4.6, the electrolyte capacitance of each pad is approximately 21nF. The charge stored at the pads is then given by the sum of the charge at each pad, calculated to be 35nC from Q = CV with V_S = 1, V_D = 0, $V_{DAu} \approx 0.35$, and $V_{SAu} \approx 0.3$ (table 3.4.1).

The most likely source of this extra charge is conduction through the previously discussed side wall connections. The much large size of the contact pads means they could reasonably store large amounts of hydrogen. Nominally, the contact pads have an Au surface, which would prevent the storage of hydrogen within the metal. However, defects in the Au or scratches from the probe tips could expose the underlying Pd layer, allowing hydrogen storage. In general, the side wall connection must be removed in order to allow quantitative predictions of device function.

Tafel Fitting

The initial current in the device is limited by the reaction:

$$PdH \rightarrow Pd + H^+ + e^-$$

The rate of this reaction is described by the Tafel equation:

$$\ln\left(\frac{I_S}{i_0}\right) = \frac{\alpha\left(V_{SInt} - V_{Eq}\right)}{V_T} \qquad \text{(eq 3.4.7)}$$

Here i_0 is exchange current density (a parameter), V_{Eq} is the equilibrium voltage of the reaction, V_T is the thermal voltage, and α is the charge transfer coefficient (another parameter). Generally, the Tafel equation describes a large number of particles impinging on a potential barrier. i_0 describes the total number of impinging particles, while α describes the probability that each particle successfully crosses the barrier. α is sensitive to the particular potential of the device. To fit this equation to the data, I rewrite it as:

$$\ln(I_S) = \frac{\alpha V_{SInt}}{V_T} - \frac{\alpha V_{Eq}}{V_T} + \ln(i_0) \qquad \text{(eq 3.4.8)}$$

On a plot of $\ln(I_S)$ against V, this is a simple linear relationship if V_{Eq} is assumed to be constant. A linear fit yields:

$$\frac{\alpha}{V_T} = Slope \qquad \text{(eq 3.4.9)}$$

$$\frac{\alpha V_{Eq}}{V_T} + \ln(i_0) = Intercept \qquad \text{(eq 3.4.10)}$$

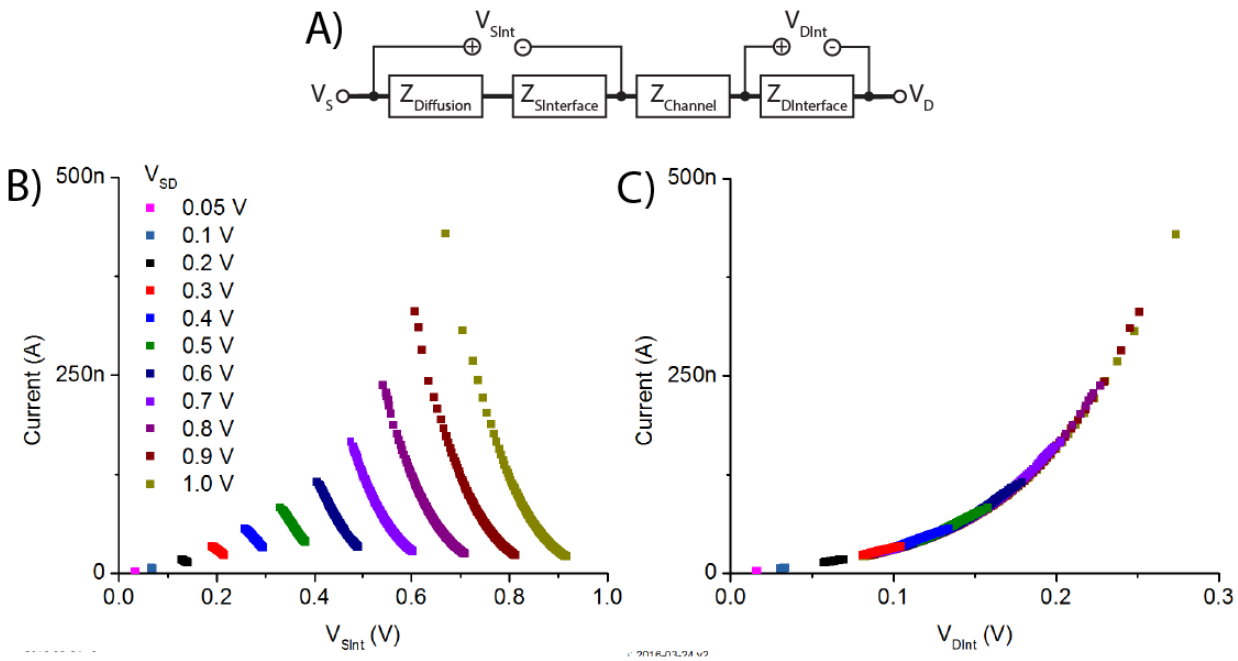

Figure 3.4.3. Parametric plots of effective device impedance. A) Schematic of the different impedances in the device. I use the the four-point probe setup to separate V_{SInt} and V_{DInt} from the channel behavior. B) Source interface I-V-t behavior. The initial current increases exponentially with voltage, as described by the Tafel equation. As time increases, the current decreases and the interface voltage increases. The final current is determined by the rate of H_2 gas absorption, and is therefore independent of voltage. C) Drain interface I-V-t behavior. As time increases, both current and voltage decrease. Generally, the total device acts as a simple voltage divider. $Z_{Diffusion}$ increases with time, and each interface has an inherently exponential I-V relationship.

Typically, V_{Eq} varies as described by the Nernst equation:

$$V_{Eq} = V_{Eq}^{0} + \frac{RT}{zF}\ln\left(\frac{a_{Ox}}{a_{Red}}\right) \qquad \text{(eq 3.4.11)}$$

However, both Pd and PdH are solids, and therefore have an activity of 1. So, the only activity that could change is that of H^+ - this is a pH dependent factor. Nafion has an extraordinarily high concentration of protons, so it is unlikely that the pH will electrostatically change during a measurement. Therefore, the Nernst equation predicts a constant V_{Eq}. Previous work by Flanagan and Lewis an explanation of the potential variations of the PdH system (*79*). They find that the electrode potential varies by a maximum of 60mV as x varies from 0 to 0.7. In particular, from x = 0.05 to x = 0.55, the potential varies by less than 10mV. Therefore, the equilibrium voltage of this reaction is roughly constant throughout the measurement, and the assumption of a constant V_{Eq} is valid.

In total, the measured devices consists of four impedances (Fig 3.4.2 A). The source contact combines diffusion ($Z_{Diffusion}$) and the Tafel reaction rate ($Z_{SInterface}$), while the drain contact has only the Tafel impedance ($Z_{DInterface}$). Compared to these impedances, the Nafion impedance ($Z_{Channel}$) is minimal. The interface voltages derived from the four point probe measurement are indicated as V_{SInt} and V_{DInt}. The relationship between current, interface voltage, and time is presented in figure 3.4.2 B and C. The initial current is the highest, with an I-V dependence described by the Tafel equation for V_S above 0.3V. Fitting this initial value yields:

$$\alpha_S = 0.13;\ \alpha_D = 0.39;\ S\ Intercept = -18.11;\ D\ intercept = -18.77$$

Below 0.3V, the Tafel equation is in the ohmic regime and displays a behavior which is linear, not exponential. As the device depletes hydrogen from the source contact, $Z_{Diffusion}$ increases exponentially, and the current decreases. As expected for a voltage divider, this causes V_{SInt} to increase and V_{DInt} to decrease. For all measurements, the final equilibrium current is limited by

the absorption rate of H_2 gas from the atmosphere. Since this diffusive process is charge neutral, the final equilibrium current is nearly independent of the applied voltage.

Simulation

I simulated the behavior of the system using the simple model shown in Figure 3.4.3 A. In this model, hydrogen is stored in the contact and Nafion layer. When a voltage is applied a proton current J_2 flows from the surface at a rate proportional to the concentration of hydrogen at the surface. As this surface layer becomes depleted, hydrogen diffuses from the surrounding environment to the surface at a rate J_1. The model parameters are the initial amount of hydrogen stored in the device (n_{init}), the initial current (J_i), and the effective combined diffusion constant (D) at which hydrogen is replenished to the surface from the Pd, Nafion, and atmosphere.

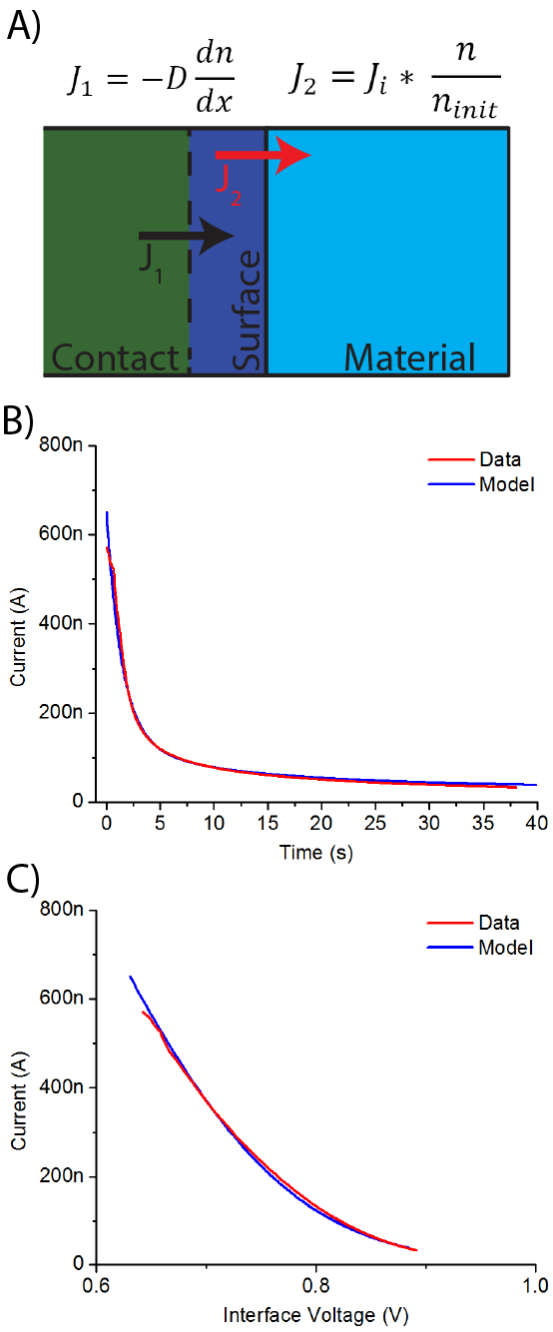

Figure 3.4.4. Simulation of the device behavior. A) Simple simulation model. J_1 is the diffusive flux of H from the contact to the surface. J_2 is the hydrogen dissociation reaction. B) Device current. The model and data agree. C) Source interface I-V relationship. I calculated the expected source interface voltage from the experimentally fitted drain interface and channel conductance behaviors.

Fitting yields J_i = 650nA, n_{init} = 2 * 10^{23} cm^{-3}, and D = 14 * 10^{-11} m^2/s, with results presented in Fig 3.4.3 B. The fitted J_i is similar to the observed current of 570nA, and the voltage dependence is calculated from the tafel equation fitting. The diffusion constant is slightly larger than that of hydrogen in Pd (4 * 10^{11} m^2/s) or Nafion (≈4 * 10^{11} m^2/s) (*77*). This increase in effective diffusion constant could also reflect the surface roughness of the material, since the average path distance from bulk to surface decreases with roughness. The fitted n_{init} is least accurate, as it describes a hydrogen density which is almost precisely three times denser than the atomic density of solid Pd. This model ignores the previously discussed leakage current at the contact pads, which is the likely source of the extra charge in the experiment.

To further verify this model, I compare it to the measured parametric depletion behavior (Fig 3.4.3 C). To calculate the effective interface voltage across the source, I use the fitted Tafel equation for the drain current, as well as the derived conductivity of the channel material. The simulated current, plotted against this derived voltage (blue) is similar to the measured behavior.

Discussion

A four-point probe measurement system with a precisely defined contact area allows greater insight into the device behavior. It allows the isolation of the interface dynamics of the metal – polymer electrolyte interface, and proves that this behavior follows the exponential Tafel relations as limited by the depletion of hydrogen from the contacts. However, the 10x difference between calculated bulk material conductivity and the literature means that further work is required to isolate the device behavior. The precisely defined contact volume and

interface area allows the separation of hydrogen stored in the contact from hydrogen absorbed from the atmosphere. The observed discrepancies in the conductivity and charge are likely caused by leakage current across the side walls of the SU-8.

Using the derived charge, I have demonstrated the separation of absorbed and stored hydrogen. The absorption rate of H_2 gas from the atmosphere is significant over the 40s measurement, with 820nC of total equivalent charge transferred to the 10um x 35um interface – a net absorption rate of 58.5 C/m^2s. Future measurements should consider this absorption rate in any estimation of the flow of hydrogen. Separately, understanding the amount of stored hydrogen helps to explain the behavior of the contact surface, although in this work the results are limited by interference from the contact pad leakage current. In addition, this leakage current interferers with the measured conductivity by coupling the Pd and Au contacts.

The measured interface behavior is less affected by the leakage current, as the observed voltage drop across the channel was generally less than 10% of the interface voltage drop. While uncertainties persist, the fitted Tafel equations are useful in demonstrating the exponential I-V relations of these interfaces. These equations will be useful in future design work, as they can be used to select device geometries with either bulk or interface dominated behavior.

I have modeled the system with a simple, two flux simulation. This model is consistent with the current, voltage, and depletion behavior of the devices. The model accurately describes the data only when it includes the excess hydrogen and 10x error in material conductivity,

experimentally caused by the leakage current. This model is a useful way to predict device behavior and verify the proposed mathematical device description.

The presented work is most limited by the leakage current at the contact pads. Future experiments should find a way to eliminate this current, perhaps with the parylene liftoff fabrication procedure described in section 3.6. In general, the methodology described in this work will allow more precise measurements of proton conducting materials, and will be useful in the design of protonic devices.

3.5 Proton Conduction in the Ampullae of Lorenzini

Reproduced with permission from Science Advances

In 1678, Stefano Lorenzini observed long, tubular structures in the Torpedo Ray (*80*). Named the Ampullae of Lorenzini (AoL) in Lorenzini's honor, these organs are also present in sharks and skates (Fig 3.5.1A, B). The function of the AoL remained a mystery for almost 300 years, until R. Murray inferred their electrosensory function in 1960 (*81*). The AoL allow sharks, skates, and rays to detect changes in electric fields generated by muscle contractions and physiology of their potential prey(*82*). An individual Ampulla consists of a pore through the skin that opens to the aquatic environment. This pore is connected to a collagen canal enclosing an epithelium that secretes a jelly like substance (AoL jelly). This canal runs sub-dermally to an alveolus that contains electrosensitive cells (*83*) (Fig. 3.5.1 C). Within the alveolus the electrosensitive cells of the Ampullae communicate with neurons (*83*). Remarkably, the integration of signals from many Ampullae allows sharks, skates, and rays to detect changes in the electric field as small as 5 nV/cm (*84-86*). It is likely that the electrical properties of the AoL jelly play a key role in this mechanism. How such weak electric fields transmit along the AoL canal to the electrosensory cells is subject to debate (*85, 86*). Different electrical properties of the AoL jelly are reported in the literature (*87-90*). The AoL jelly is either reported as a semiconductor with temperature dependence conductivity and thermoelectric behavior(*87, 88*), or as a simple ionic conductor with the same electrical properties as the surrounding seawater(*89, 90*). Here, using proton conducting devices, I demonstrate that the AoL jelly is a remarkable proton conducting material and speculate that the polyglycans contained in the AoL jelly may contribute its proton conductivity.

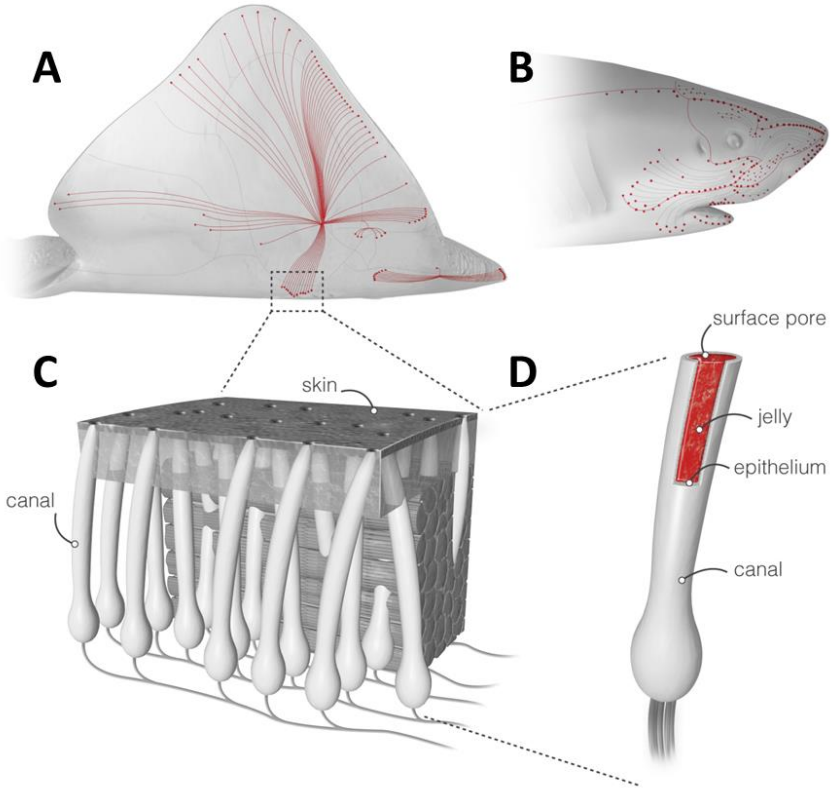

Figure 3.5.1 The Ampullae of Lorenzini **A, B**) Skates and Sharks locate their prey by detecting the weak electric fields naturally generated by biomechanical activity. **C)** A network of electrosensory organs called the Ampullae of Lorenzini is responsible for this sense **D**) An individual ampulla consists of a surface pore connected to a set of electrosensory cells by a long jelly-filled canal. Sharks and skate can sense fields as small as 5nV/cm despite canals traveling through up to 25 cm of noisy biological tissue.

DC Electrical Measurements with PdH_x proton conducting contacts

I performed initial electrical measurements in a standard two-terminal geometry with palladium (Pd) source and drain contacts (Fig 3.5.2A) (*15, 41, 91, 92*). When Pd is exposed to hydrogen, Pd forms palladium hydride (PdH_x) with a stoichiometric ratio $x \leq 0.6$. With a source-drain potential difference,

V_{SD}, the PdH_x source and drain inject and drain protons (H^+) into and from the AoL jelly samples, effectively serving as protodes (*15, 41, 91, 92*). For each H^+ injected into the AoL jelly, an excess electron is collected by the leads, which complete the circuit and result in a current measured at the drain, I_D (Fig 3.5.2A). For an applied V_{SD}= 1 V, I measured I_D at room temperature as a function of time (t) in an atmosphere of nitrogen or hydrogen with controlled relative humidity (RH), as previously described for the biopolymer melanin(*12*). For RH= 50%, the AoL jelly samples extracted from *Raja rhina* have very low electrical conductivity with I_D ~ 3 nA when measured with electrically conducting and proton blocking Pd contacts exposed to nitrogen (Fig 3.5.2B, black curve). At low RH, the only contribution to I_D is likely from electrons, because ions and protons require a highly hydrated material in order to conduct(*21*). For RH= 75%, I_D increases with a 10 nA peak when measured with Pd contacts (Fig 3.5.2B, blue curve). The formation of a Debye layer from the ions blocked at the contact- AoL jelly interface causes I_D to rapidly decrease to 0.3 nA at t= 20 s. Since Pd contacts are blocking ions and protons, I_D= 10 nA is likely the ionic component to the transient current in the AoL jelly, which contains the same ionic species as seawater(*90*) (*Table S1*). The observed capacitance (22nF) is consistent with the estimated capacitance for ionic charging of the Pd-AoL Jelly interface (26nF). Similar behavior has been observed for ionic currents in the biopolymer melanin(*12*). This ionic component corresponds to an ionic conductivity of the AoL jelly, σ_{ion}= 100 nS/cm. This σ_{ion} is rather low compared to the conductivity of seawater (≈40 mS/cm), which was also attributed to the AoL jelly by prior work(*90*). However, larger ions such as Na^+ and Cl^- require larger pores in the material to be able to diffuse, and low ionic conductivity of the AoL jelly was also previously observed (*93*). For proton conducting PdH_x contacts at 75% RH,

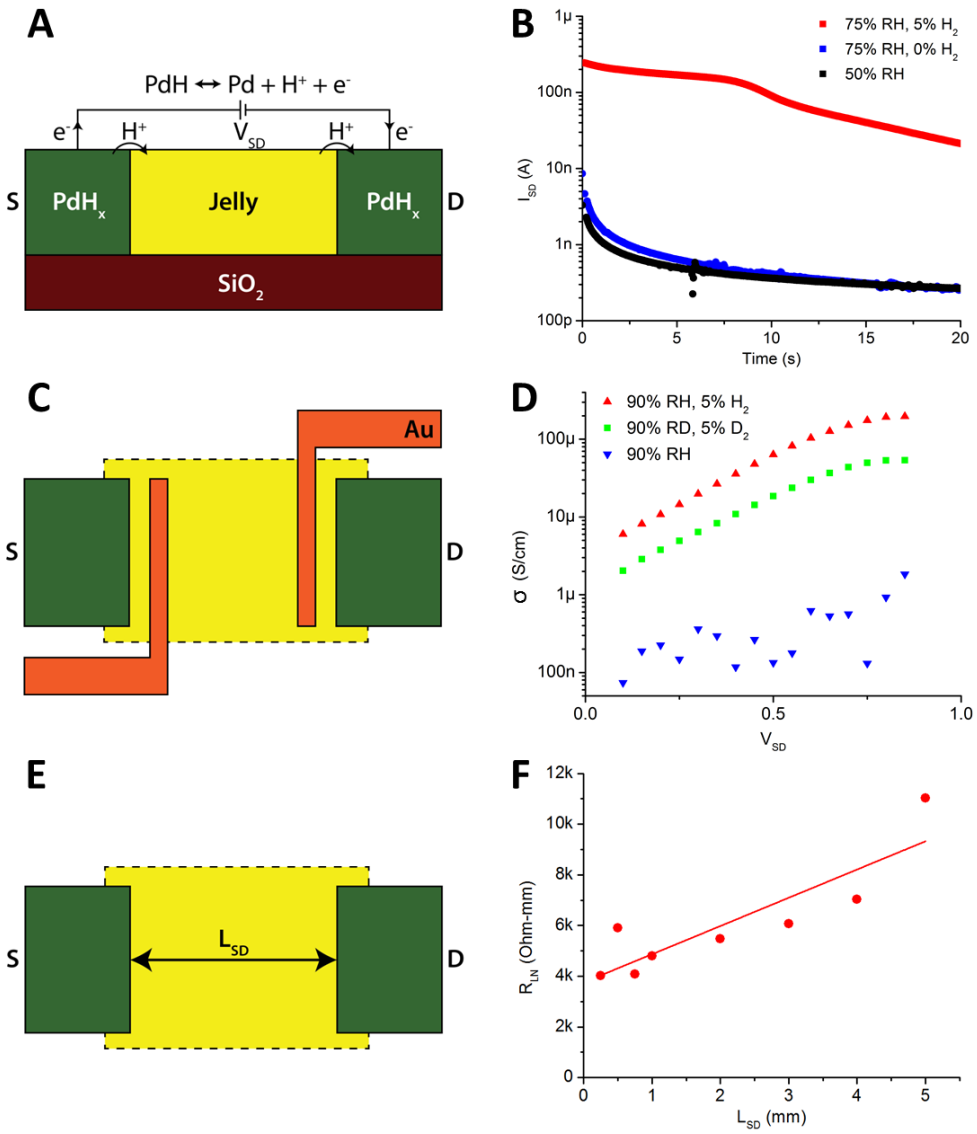

Figure 3.5.2. Proton Conduction in Ampullae Jelly. **A**) Palladium hydride protode behavior. Under an applied voltage, PdH contacts split into Pd, H+, and e-. Protons are injected into the skate jelly, while electrons travel through external circuitry and are measured. **B)** Transient response to a 1V applied signal in AoL jelly from Raja rhina. The proton current (red) is 50x larger than the ion current (blue). The electron current (black) is slightly smaller than the ion current. **C)** Four-point probe geometry. Distinct Au contacts are used to measure voltage within the channel and correct for any

potential drop at the PdH-jelly interface. **D)** Four-point probe conductivity results from Raja binoculata. Conductivity increases exponentially with voltage up to about 1V, suggesting that conduction is limited by potential barriers. Deuterium conductivity (green) at 90% D_2O humidity (RD) is half as large as proton conductivity (red) for all voltages. Ion conduction in the hydrated state (blue) is minimal. **E)** Transmission Line Measurement (TLM) geometry. Varying the distance between source and drain (L_{SD}) distinguishes between the fixed PdH-jelly interface resistance and the varying bulk resistance. **F)** R_{LN} as a function of L_{SD} for Raja binoculata. A linear fit gives a bulk material proton conductivity of 1.8 ± 0.9mS/cm.

I_D peaks at 250nA, indicating a strong component of proton conductivity (Fig 3.5.2B, red trace). This proton conductivity is consistent with the activation energy for the conductivity of shark Ampullae of Lorenzini jelly (*90*). With PdH_x contacts, I_D drops over time. At first sight, this time dependence may suggest proton blocking behavior at the contact. However, I observed similar time dependence when measuring highly proton conducting materials such as Nafion with PdH_x contacts (*91*). This time dependence arises when the diffusion of hydrogen to the PdH_x contact surface is slower than the conduction of H^+ in the proton conducting material (*91*).

Four Point Probe Measurement and Kinetic Isotope Effect

The injection of protons from the contact into the AoL jelly incurs a significant contact resistance, and the depletion of H at the PdH_x contacts causes a drop in I_D as previously observed (*91*). To circumvent these issues, I used a modified four-point probe geometry to measure the proton conductivity (σ_{H+}) of the AoL jelly independently of the PdH_x- AoL jelly contact resistance. In this geometry, I added two thin Au contacts between the Pd source and

drain, for a total of four contacts. When I apply V_{SD} to the PdH_x source and drain, a current of H^+ flows in the AoL jelly as demonstrated in the standard two-probe geometry. I measured the potential difference between the two Au contacts. This potential difference is proportional to I_D and inversely proportional to the conductivity of the AoL jelly (Fig 3.5.2C). Since no current flows across the Au-AoL jelly interface, there is no potential drop and the PdH_x contact resistance does not affect the measurement of the conductivity of the AoL jelly. For Pd contacts at 90% RH, I find $\sigma_{ion} \approx$ 100 - 1000 nS/cm depending on V_{SD} (Fig 3.5.2D, blue trace), which is consistent with my observations in the two-probe geometry (Fig. 3.5.2B). For PdH_x contacts at 90% RH, I find $\sigma_{H+} \approx$ 6 - 200 µS/cm, peaking at 200 µS/cm for V_{SD}= 1V (Fig 3.5.2D, red trace). This conductivity is similar to that of dialyzed AoL jelly from a shark in a DC measurement (800 µS/cm) (*90*). In these measurements, the proton conductivity of the AoL jelly depends exponentially on V_{SD}, which is similar to the highly proton conducting polymer Nafion (*94*). To confirm that the AoL jelly conductivity indeed arises from H^+, I repeated the measurements by hydrating the sample with deuterated water and by exposing the Pd to deuterium rather than to hydrogen. Deuterium ions (D^+) transport along hydrated materials in a similar fashion as protons, but with a lower mobility and associated lower conductivity (*95*). Hydrating the AoL jelly samples with D_2O substitutes D^+ for H^+ in the material. A subsequent decrease in conductivity for D^+ (σ_{D+}) – the kinetic isotope effect – is a well-accepted signature for conductivity arising predominantly from protons (*95*). For the AoL jelly, $\sigma_{D+} = ½\ \sigma_{H+}$ for any V_{SD} when measured in the four point probe geometry (Fig. 3.5.2D, green trace). The kinetic isotope effect with this four point probe measurement unequivocally points to proton conduction in the AoL jelly (*95*). However, these measurements likely underestimates the AoL

jelly conductivity (σ_{H+}= 0.2 ms/cm). In the four-point probe geometry, I find the proton conductivity of Nafion at σ_{H+}= 2 mS/cm, which is lower than the literature value (σ_{H+}= 78 mS/cm) (*43*). This measured conductivity of the Nafion control sample is smaller than expected. I suspect that non-ideal geometry is the cause of this variation. The calculated conductivity assumes that only the material in the channel is relevant to conduction, since the electric field is highest here. However, if the interface resistance is comparable to the channel resistance, this assumption may not be accurate, skewing the calculated results (*69*). To address this variation, I measured the proton conductivity of the AoL jelly in a transmission line geometry.

Discussion

With two and four terminal devices using proton-conducting PdH_x contacts I measured the proton conductivity of the jelly extracted from the Ampullae of Lorenzini of skates and sharks. The proton conductivity of the Ampullae of Lorenzini jelly is as high as σ_{H+}=2 mS/cm. This value is the highest reported for the proton conductivity of any biological material, and it is only forty times lower than the proton conductivity for Nafion, the current state-of-the-art polymer proton conductor. With the assistance of Pegah Hassanzadeh, I performed preliminary characterization of the Ampullae of Lorenzini jelly, reconfirming the presence of the polyglycan keratan sulfate. I propose that the high proton conductivity of the Ampullae of Lorenzini jelly may arise from protons donated by the keratan sulfate acid groups to the water contained in the hydrated jelly. This high proton conductivity of the Ampullae of Lorenzini jelly is remarkable and I hope that the observation of this conductivity may contribute to future studies of the Ampullae of Lorenzini electrosensing function.

3.6 Carbon Nanotube Protonics

Carbon nanotubes have aspect ratios greater than 10,000, and directly connect the micro-scale to the nano-scale. CNTs are heavily researched for electronic applications, and may help continue Moore's law into the quantum regime. Their minute size minimizes the energy required for switching, while their geometrically tunable band structure allows optimization of device parameters(*96*). In addition to their well-known electronic applications, recent work has introduced CNTs as diameter-selective nanopores. Holt et. al. showed a large-area SiN membrane spanned by CNTs(*97*), while Sun et. al. demonstrated a single-CNT membrane(*98*). Results from such devices show conduction rates 5 order of magnitude higher than expected from traditional fluid dynamics for both fluids and gases(*99*). These observations launched the nascent field of nanofluidics, a nano-scale complement to microfluidics which intends to fully realize the selectivity and conductivity of CNTs(*100*).

To explain the anomalous fluid flow through a CNT, Koga et. al simulated the filling of water inside a CNT(*101*). They found that water forms a regular, ice-like structure, with the uniform internal potential of the nanotube allowing rapid flow. This ordered structure is remarkably similar to the ordered chain of water molecules in gramicidin (Figure 1)(*57*). Due to their similarity, CNTs are therefore also expected to conduct protons(*18*), and might serve as a controlled artificial gramicidin(*102*).

Gramicidin is an antibiotic that functions by integrating with a cell membrane and causing a rapid flow of protons(*2*). This disrupts the transmembrane proton gradient that all cells maintain as a fundamental form of energy storage. A cell's proton gradient is created by

metabolic activity like the actions of photosystem 1(*103*), and used for everything from signaling to ATP production(*52*). Like gramicidin, CNTs will naturally integrate with cell membranes due to their hydrophobic exterior and hydrophilic ends(*104*). Therefore, the high selectivity of ensemble membranes might be applied to novel nanomedical applications in single CNTs (Figure 2). However, if CNTs are to act as anything but a cell-killing antibiotic, their proton conductivity must be understood and controlled.

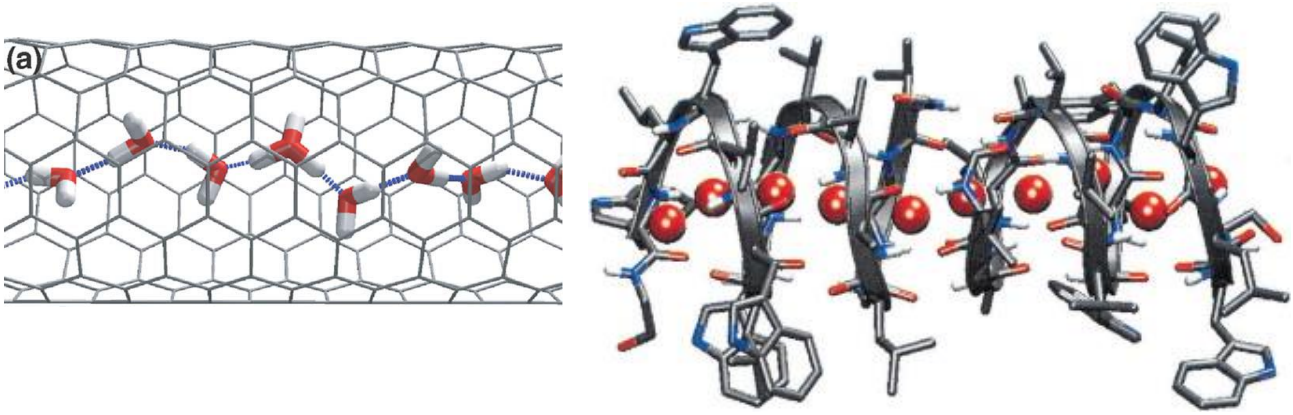

Figure 3.6.1. Theory of proton conduction in carbon nanotubes. Left: Molecular dynamics simulations predict that the core of the CNT will fill with a chain of water molecules in a hydrogen bonded chain(*18*). Right: The structure of gramicidin, an antibiotic and highly efficient proton conductor(*2*).

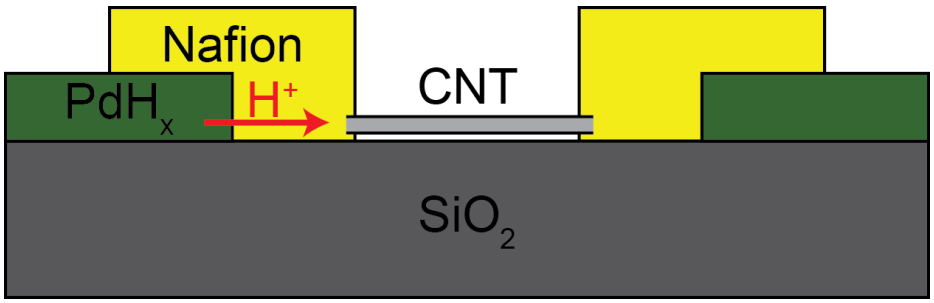

Figure 3.6.2. The proposed Nafion-CNT device for proton conduction measurements. PdH_x contacts act as a proton supply. Nafion pads conduct the protons to the target device while preventing the flow of electrons.

I made significant initial progress in fabricating a CNT-channel protonic device using the geometry shown in Figure 3.6.2. The PdH_x contacts act as protodes, injecting protons into the Nafion layer. The Nafion layer is an electron filter that isolates the otherwise conductive CNT from the metal contacts. Since the conductivity of Nafion is high, this layer should not limit the proton flux through the nanotube, although interface effects may be significant. The nanotube spans an open gap between the Nafion, with total length between 2 and 10 um. Proton current flows from the protodes, through the Nafion, and into the CNT core. Ideally, CNT conduction is the limiting factor in current flow and the resistance of the PdH_x and Nafion are small in comparison.

This design has several advantages over previous works. The CNT is not covered by any other layer, guaranteeing that no alternate conduction pathways exist through the barrier layer. Since the CNT is exposed, it can be easily characterized both before and after measurements. And, this exposure may allow extra functionalization of the CNT surface, as demonstrated by the Noy group(*10, 105*).

The fabrication of this device is limited by several constraints. First, it is important that no ions contaminate the device. Otherwise, they may unpredictably alter the behavior, as seen in previous work(*106*). Therefore, once the CNT is opened, no exposure to ion-rich process chemicals is allowed. Further, the Nafion layer must also be kept free from ions, prohibiting the use of standard photolithographic liftoff to pattern it. And, any temperatures above 150°C cross the glass transition temperature of Nafion and lower the proton conductivity(*107*). However, some form of patterning is required to ensure good-quality devices with a short channel length.

To solve these constraints, I fabricated this device with a parylene peel-off process (Figure 3.6.3)([108, 109]). First introduced for the patterning of sensitive biomaterials, this process uses an etched parylene layer as an adhered shadowmask. Parylene C is deposited on the surface under low vacuum, forming a layer 2-3µm thick. Photolithography and a reactive plasma are then used to pattern and etch the layer. With the layer formed, a sample solution is placed on the surface, and the suspended material allowed to settle. Then, the parylene layer is mechanically peeled away. This leaves the behind the patterned material without ever introducing it to harsh chemicals, or even leaving the solution. I used parylene liftoff to pattern the Nafion in the Nafion-CNT devices. This keeps the CNTs protected during fabrication, while also self-aligning the CNT etch to the Nafion deposition. The full fabrication procedure is given in Figure 3.6.3.

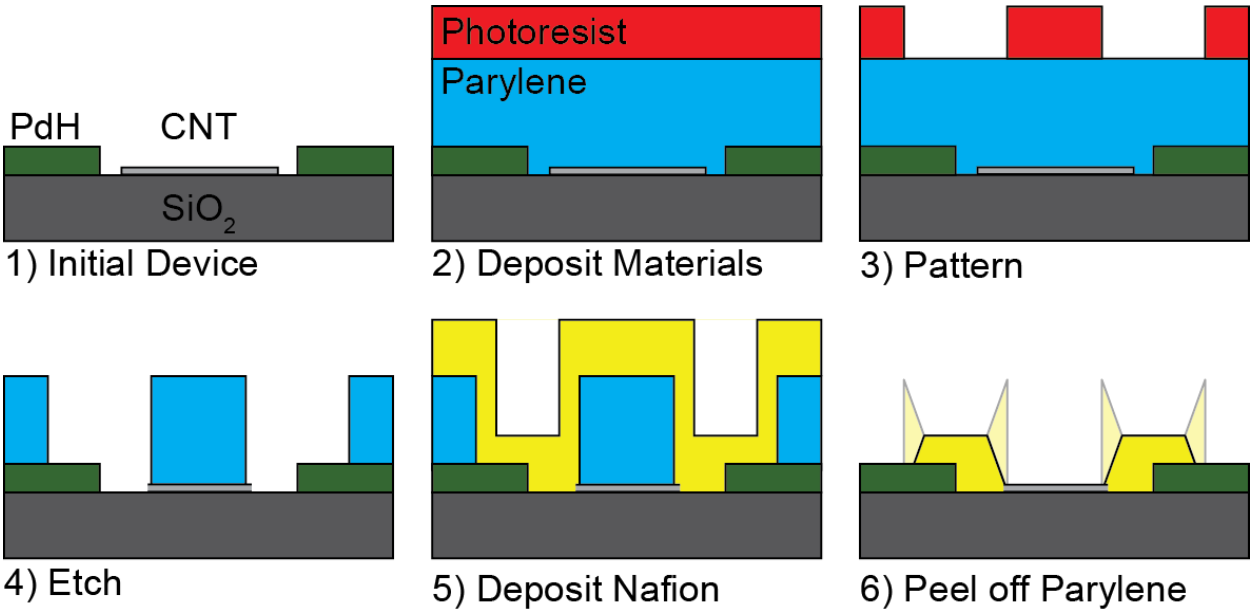

Figure 3.6.3. The proposed fabrication method for the Nafion-CNT devices. Steps are discussed in detail in the text.

In this project, I collaborated with professor Aleksandr Noy, who created single-walled CNTs on a 100nm thick SiO_2 surface through flow-aligned CVD deposition. The size and chirality of the CNTs is determined by the CVD parameters(*110*). When first created, the CNTs are capped with fullerenes and insensitive to contamination. Therefore, standard contact lithography can be used to deposit PdHx electrodes on the device (3.6.3.1).

Next, I coated the samples with parylene through vapor phase deposition (3.6.3.2). Here, a parylene dimer precursor is sublimated, and then pyrolized into the monomer form. The monomer gas then deposits on the cool sample surfaces. The thickness of the parylene layer is easily controlled by the mass of precursor vaporized. After deposition, the parylene layer is covered with a photoresist layer, which is patterned with contact lithography (3.6.3.2).

The device is etched in an inductively coupled plasma reactive ion etcher, with high anisotropy (3.6.3.4). This etch opens the required holes in the parylene, and also opens the CNT ends. The etch gases are a 3:1 mix of O_2:N_2, which is expected to result in –COOH terminations on the CNT ends. The photoresist is also etched by this process. To prevent contamination, I chose the photoresist such that the last photoresist is etched away while 10-15% of the parylene is still remaining. This keeps the CNT ends protected from any contact with the photoresist.

After etching, the devices will be coated with Nafion (3.6.3.5). Drop-casting yields 1-3µm thick, non-uniform film that lifts off poorly due to strong parylene side-wall connections. Therefore, I used spin-coating to generate a more uniform, 100-400nm film of Nafion. As expected, the thickness of the Nafion film is proportional to the spin speed. Reducing the film thickness weakens the connection between layers and minimizes mechanical damage to the film.

Lastly, the parylene layer is peeled away (3.6.3.6). This is performed with tweezers under an optical microscope (figure 19). The peel direction is chosen to ensure consistent tearing. After peeling, the device is ready for measurement and characterization.

I successfully patterned Nafion films with high resolution and low feature size using this fabrication process (Figure 3.6.4). The devices had some small amount of sidewall tearing, but not enough to interfere with device function. Unfortunately, my collaborator had issues in providing nanotubes with the required length. In addition, the measured conductivity of the control devices was significantly lower than expected. In conjunction with the AoL jelly behavior, this highlights the need for a better understanding of the PdH – material behavior. Therefore, I have pursued this study to enable future works.

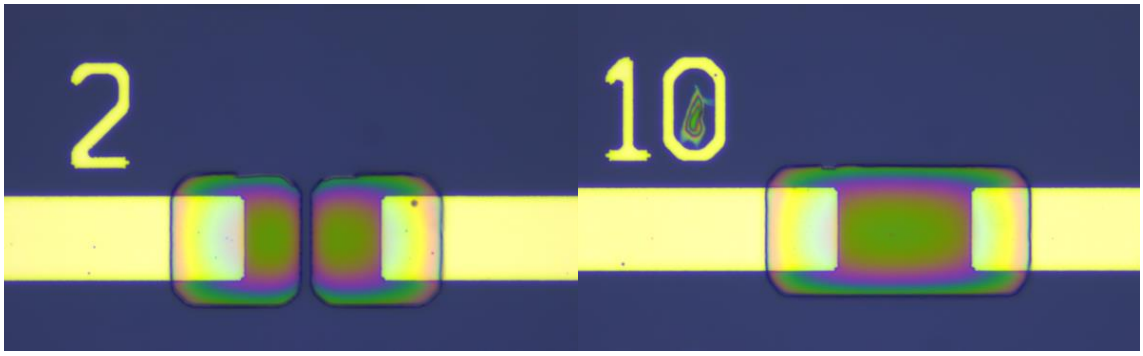

Figure 3.6.4. Successful devices from a fabrication test run without CNTs. Device 2 has a 2µm gap between the Nafion pads, while device 10 is a control device with the Nafion pads intentionally connected. Minor tearing of the Nafion occurred during parylene liftoff, but not enough to interfere with device function.

4. Outlook

The measurement and control of proton motion may allow dramatic new sensors and bioengineering capabilities. Modifying materials like chitosan allows for complementary proton conducting materials, with inherent functionality. Control of the PdH contact geometry expands this functionality with optional memory elements, for basic information processing and storage. These PdH contacts can be formed or depleted electrochemically from solution, which may allow devices that function without a supply of hydrogen gas. I have described the behavior of the PdH – polymer interface with high precision, allowing better design of future measurements. I have discovered a natural proton conducting material used in electrosensing. The methods and results I describe, combined with carbon nanotube protonic devices, may allow the future fabrication of wholly artificial proton pores, representing the first creation of artificial devices for direct use in cellular systems.

BIBLIOGRAPHY

1. T. Nishi, M. Forgac, The vacuolar (H+)-ATPases—nature's most versatile proton pumps. *Nature reviews Molecular cell biology* **3**, 94-103 (2002).
2. R. Pomes, B. Roux, Molecular mechanism of H+ conduction in the single-file water chain of the gramicidin channel. *Biophys J* **82**, 2304-2316 (2002); published online EpubMay (
3. J. A. Wemmie, M. P. Price, M. J. Welsh, Acid-sensing ion channels: advances, questions and therapeutic opportunities. *Trends in neurosciences* **29**, 578-586 (2006).
4. J. Du, L. R. Reznikov, M. P. Price, X.-m. Zha, Y. Lu, T. O. Moninger, J. A. Wemmie, M. J. Welsh, Protons are a neurotransmitter that regulates synaptic plasticity in the lateral amygdala. *Proceedings of the National Academy of Sciences* **111**, 8961-8966 (2014).
5. R. M. Owens, G. G. Malliaras, Organic electronics at the interface with biology. *MRS bulletin* **35**, 449-456 (2010).
6. A. Noy, Bionanoelectronics. *Advanced Materials* **23**, 807-820 (2011).
7. D. Nilsson, M. Chen, T. Kugler, T. Remonen, M. Armgarth, M. Berggren, Bi-stable and dynamic current modulation in electrochemical organic transistors. *Advanced Materials* **14**, 51-54 (2002).
8. M. Chen, D. Nilsson, T. Kugler, M. Berggren, T. Remonen, Electric current rectification by an all-organic electrochemical device. *Applied physics letters* **81**, 2011-2013 (2002).
9. K. Svennersten, K. C. Larsson, M. Berggren, A. Richter-Dahlfors, Organic bioelectronics in nanomedicine. *Biochimica et Biophysica Acta (BBA)-General Subjects* **1810**, 276-285 (2011).
10. S.-C. J. Huang, A. B. Artyukhin, N. Misra, J. A. Martinez, P. A. Stroeve, C. P. Grigoropoulos, J.-W. W. Ju, A. Noy, Carbon Nanotube Transistor Controlled by a Biological Ion Pump Gate. *Nano Letters* **10**, 1812-1816 (2010); published online Epub2010/05/12 (10.1021/nl100499x).
11. J. Geng, K. Kim, J. Zhang, A. Escalada, R. Tunuguntla, L. R. Comolli, F. I. Allen, A. V. Shnyrova, K. R. Cho, D. Munoz, Y. M. Wang, C. P. Grigoropoulos, C. M. Ajo-Franklin, V. A. Frolov, A. Noy, Stochastic transport through carbon nanotubes in lipid bilayers and live cell membranes. *Nature* **514**, 612-615 (2014).
12. J. Wünsche, Y. Deng, P. Kumar, E. Di Mauro, E. Josberger, J. Sayago, A. Pezzella, F. Soavi, F. Cicoira, M. Rolandi, Protonic and electronic transport in hydrated thin films of the pigment eumelanin. *Chemistry of Materials* **27**, 436-442 (2015).
13. D. D. Ordinario, L. Phan, W. G. Walkup IV, J.-M. Jocson, E. Karshalev, N. Hüsken, A. A. Gorodetsky, Bulk protonic conductivity in a cephalopod structural protein. *Nature chemistry* **6**, 596-602 (2014).
14. N. Amdursky, X. Wang, P. Meredith, D. D. Bradley, M. M. Stevens, Long-Range Proton Conduction across Free-Standing Serum Albumin Mats. *Advanced Materials*, (2016).
15. C. Zhong, Y. Deng, A. F. Roudsari, A. Kapetanovic, M. P. Anantram, M. Rolandi, A polysaccharide bioprotonic field-effect transistor. *Nat Commun* **2**, 476 (2011)http://www.nature.com/ncomms/journal/v2/n9/suppinfo/ncomms1489_S1.html).
16. C. A. Wraight, Chance and design - Proton transfer in water, channels and bioenergetic proteins. *Bba-Bioenergetics* **1757**, 886-912 (2006); published online EpubAug (DOI 10.1016/j.bbabio.2006.06.017).
17. M. Eigen, L. Demaeyer, Self-Dissociation and Protonic Charge Transport in Water and Ice. *Proc R Soc Lon Ser-A* **247**, 505-533 (1958)DOI 10.1098/rspa.1958.0208).
18. C. Dellago, M. M. Naor, G. Hummer, Proton transport through water-filled carbon nanotubes. *Phys Rev Lett* **90**, (2003); published online EpubMar 14 (Artn 105902 Doi 10.1103/Physrevlett.90.105902).

19. J. F. Nagle, M. Mille, H. J. Morowitz, Theory of Hydrogen-Bonded Chains in Bioenergetics. *J Chem Phys* **72**, 3959-3971 (1980).
20. E. J. Murphy, Ionic-Conduction in Keratin (Wool). *Journal of Colloid and Interface Science* **54**, 400-408 (1976).
21. Bardelme.Gh, Electrical-Conduction in Hydrated Collagen .1. Conductivity Mechanisms. *Biopolymers* **12**, 2289-2302 (1973).
22. H. Morgan, R. Pethig, G. T. Stevens, A Proton-Injecting Technique for the Measurement of Hydration-Dependent Protonic Conductivity. *J Phys E Sci Instrum* **19**, 80-82 (1986); published online EpubJan (
23. J. W. Hanneken, Ph.D. thesis, Rice University, Houston, Texas (1978).
24. D. B. Strukov, G. S. Snider, D. R. Stewart, R. S. Williams, The missing memristor found (vol 453, pg 80, 2008). *Nature* **459**, - (2009); published online EpubJun 25 (Doi 10.1038/Nature08166).
25. M. Di Ventra, Y. V. Pershin, L. O. Chua, Circuit Elements With Memory: Memristors, Memcapacitors, and Meminductors. *P Ieee* **97**, 1717-1724 (2009); published online EpubOct (Doi 10.1109/Jproc.2009.2021077).
26. F. Xiong, A. D. Liao, D. Estrada, E. Pop, Low-Power Switching of Phase-Change Materials with Carbon Nanotube Electrodes. *Science* **332**, 568-570 (2011).
27. S. H. Jo, T. Chang, I. Ebong, B. B. Bhadviya, P. Mazumder, W. Lu, Nanoscale memristor device as synapse in neuromorphic systems. *Nano Letters* **10**, 1297-1301 (2010); published online EpubApr 14 (10.1021/nl904092h).
28. Q. X. Lai, L. Zhang, Z. Y. Li, W. F. Stickle, R. S. Williams, Y. Chen, Ionic/Electronic Hybrid Materials Integrated in a Synaptic Transistor with Signal Processing and Learning Functions. *Advanced Materials* **22**, 2448-+ (2010); published online EpubJun 11 (Doi 10.1002/Adma.201000282).
29. S. Ramakrishnan, P. E. Hasler, C. Gordon, Floating Gate Synapses With Spike-Time-Dependent Plasticity. *Ieee T Biomed Circ S* **5**, 244-252 (2011); published online EpubJun (Doi 10.1109/Tbcas.2011.2109000).
30. Z.-L. Xu, F. Alsalhy Qusay, Polyethersulfone (PES) hollow fiber ultrafiltration membranes prepared by PES/non-solvent/NMP solution. *Journal of Membrane Science* **233**, 101-111 (2004); published online Epub4/15/ (http://dx.doi.org/10.1016/j.memsci.2004.01.005).
31. K. Kim, C. L. Chen, Q. Truong, A. M. Shen, Y. Chen, A Carbon Nanotube Synapse with Dynamic Logic and Learning. *Advanced Materials* **25**, 1693-1698 (2013); published online EpubMar 25 (DOI 10.1002/adma.201203116).
32. J. Shi, S. D. Ha, Y. Zhou, F. Schoofs, S. Ramanathan, A correlated nickelate synaptic transistor. *Nature Communications* **4**, 2676 (2013); published online EpubNov 1 (10.1038/ncomms3676).
33. A. Thomas, Memristor-based neural networks. *J Phys D Appl Phys* **46**, (2013); published online EpubMar 6 (Artn 093001 Doi 10.1088/0022-3727/46/9/093001).
34. J. B. Lont, W. Guggenbuhl, Analog Cmos Implementation of a Multilayer Perceptron with Nonlinear Synapses. *Ieee T Neural Networ* **3**, 457-465 (1992); published online EpubMay (Doi 10.1109/72.129418).
35. D. Kuzum, R. G. D. Jeyasingh, B. Lee, H. S. P. Wong, Nanoelectronic Programmable Synapses Based on Phase Change Materials for Brain-Inspired Computing. *Nano Letters* **12**, 2179-2186 (2012); published online EpubMay (Doi 10.1021/Nl201040y).
36. R. S. Zucker, W. G. Regehr, Short-term synaptic plasticity. *Annu Rev Physiol* **64**, 355-405 (2002)Doi 10.1146/Annurev.Physiol.64.092501.114547).
37. V. V. Zhirnov, R. K. Cavin, Nanodevices: Charge of the heavy brigade. *Nat Nanotechnol* **3**, 377-378 (2008); published online EpubJul (Doi 10.1038/Nnano.2008.197).

38. D. B. Strukov, J. L. Borghetti, R. S. Williams, Coupled Ionic and Electronic Transport Model of Thin-Film Semiconductor Memristive Behavior. *Small* **5**, 1058-1063 (2009); published online EpubMay 4 (Doi 10.1002/Smll.200801323).
39. R. S. Zucker, Short-Term Synaptic Plasticity. *Annu Rev Neurosci* **12**, 13-31 (1989)DOI 10.1146/annurev.neuro.12.1.13).
40. L. Glasser, Proton Conduction and Injection in Solids. *Chemical Reviews* **75**, 21-65 (1975).
41. Y. Deng, E. Josberger, J. Jin, A. F. Rousdari, B. A. Helms, C. Zhong, M. P. Anantram, M. Rolandi, H+-type and OH--type biological protonic semiconductors and complementary devices. *Sci. Rep.* **3**, 2481 (2013)10.1038/srep02481).
42. R. C. T. Slade, J. Barker, J. H. Strange, Protonic Conduction and H-1 Self-Diffusion in Nafion Film Studied by Ac Conductivity and Pulsed Field Gradient Nmr Techniques. *Solid State Ionics* **35**, 11-15 (1989); published online EpubJul-Aug (
43. Y. Sone, P. Ekdunge, D. Simonsson, Proton conductivity of Nafion 117 as measured by a four-electrode AC impedance method. *Journal of the Electrochemical Society* **143**, 1254-1259 (1996); published online EpubApr (Doi 10.1149/1.1836625).
44. P. Choi, N. H. Jalani, R. Datta, Thermodynamics and proton transport in Nafion - II. Proton diffusion mechanisms and conductivity. *Journal of the Electrochemical Society* **152**, E123-E130 (2005)Doi 10.1149/1.1859814).
45. T. H. Yang, S. Pyun, Y. Yoon, Hydrogen transport through Pd electrode: Current transient analysis. *Electrochim Acta* **42**, 1701-1708 (1997)Doi 10.1016/S0013-4686(96)00369-6).
46. G. M. Shepherd, *Neurobiology*. (Oxford University Press, ed. Third, 1994).
47. H. J. Koo, J. H. So, M. D. Dickey, O. D. Velev, Towards All-Soft Matter Circuits: Prototypes of Quasi-Liquid Devices with Memristor Characteristics. *Advanced Materials* **23**, 3559-+ (2011); published online EpubAug 16 (DOI 10.1002/adma.201101257).
48. B. Z.-N. Heinrich Reichert, *Introduction to Neurobiology*. (Oxford University Press, 1992).
49. R. Waser, M. Aono, Nanoionics-based resistive switching memories. *Nature Materials* **6**, 833-840 (2007); published online EpubNov (
50. T. E. DeCoursey, Voltage-gated proton channels and other proton transfer pathways (vol 83, pg 475, 2003). *Physiological Reviews* **83**, 1067-1067 (2003); published online EpubJul (Doi 10.1152/Physrev.00028.2002).
51. P. Mitchell, Chemiosmotic coupling in oxidative and photosynthetic phosphorylation. *Biol Rev Camb Philos Soc* **41**, 445-502 (1966); published online EpubAug (
52. H. J. Morowitz, Proton Semiconductors and Energy Transduction in Biological-Systems. *Am J Physiol* **235**, R99-R114 (1978).
53. J. K. Lanyi, Bacteriorhodopsin. *Annu Rev Physiol* **66**, 665-688 (2004)Doi 10.1146/Annurev.Physiol.66.032102.150049).
54. S. M. Smith, D. Morgan, B. Musset, V. V. Cherny, A. R. Place, J. W. Hastings, T. E. Decoursey, Voltage-gated proton channel in a dinoflagellate. *Proc Natl Acad Sci U S A* **108**, 18162-18167 (2011); published online EpubNov 1 (10.1073/pnas.1115405108 1115405108 [pii]).
55. D. Walz, S. R. Caplan, Bacterial flagellar motor and H+/ATP synthase: two proton-driven rotary molecular devices with different functions. *Bioelectrochemistry* **55**, 89-92 (2002); published online EpubJan (Pii S1567-5394(01)00162-1 Doi 10.1016/S1567-5394(01)00162-1).
56. M. Capasso, T. E. DeCoursey, M. J. S. Dyer, pH regulation and beyond: unanticipated functions for the voltage-gated proton channel, HVCN1. *Trends in cell biology* **21**, 20-28 (2011).
57. D. Busath, G. Szabo, Gramicidin forms multi-state rectifying channels. *Nature* **294**, 371-373 (1981); published online EpubNov-Dec (
58. S. Cukierman, Et tu, Grotthuss! and other unfinished stories. *Bba-Bioenergetics* **1757**, 876-885 (2006); published online EpubAug (Doi 10.1016/J.Bbabio.2005.12.001).

59. J. F. Nagle, M. Mille, H. J. Morowitz, Theory of Hydrogen-Bonded Chains in Bioenergetics. *Biophys J* **25**, A48-A48 (1979).
60. J. F. Nagle, H. J. Morowitz, Molecular Mechanisms for Proton Transport in Membranes. *P Natl Acad Sci USA* **75**, 298-302 (1978)Doi 10.1073/Pnas.75.1.298).
61. D. Riccardi, P. Konig, X. Prat-Resina, H. B. Yu, M. Elstner, T. Frauenheim, Q. Cui, "Proton holes" in long-range proton transfer reactions in solution and enzymes: A theoretical analysis. *J Am Chem Soc* **128**, 16302-16311 (2006); published online EpubDec 20 (Doi 10.1021/Ja065451j).
62. B. Musset, S. M. E. Smith, S. Rajan, D. Morgan, V. V. Cherny, T. E. DeCoursey, Aspartate 112 is the selectivity filter of the human voltage-gated proton channel. *Nature* **480**, 273-U167 (2011); published online EpubDec 8 (Doi 10.1038/Nature10557).
63. C. Zhong, A. Kapetanovic, Y. Deng, M. Rolandi, Nanofiber Ink: A Chitin Nanofiber Ink for Airbrushing, Replica Molding, and Microcontact Printing of Self-assembled Macro-, Micro-, and Nanostructures (Adv. Mater. 41/2011). *Advanced Materials* **23**, 4720-4720 (2011).
64. A. Cooper, C. Zhong, Y. Kinoshita, R. S. Morrison, M. Rolandi, M. Zhang, Self-assembled chitin nanofiber templates for artificial neural networks. *Journal of Materials Chemistry* **22**, (2012).
65. A. Francesko, T. Tzanov, Chitin, chitosan and derivatives for wound healing and tissue engineering. *Adv Biochem Eng Biotechnol* **125**, 1-27 (2011)10.1007/10_2010_93).
66. J. H. Christie, I. M. Woodhead, A new model of DC conductivity of hygroscopic solids - Part 1: Cellulosic materials. *Textile Research Journal* **72**, 273-278 (2002); published online EpubMar (
67. V. M. Volgin, A. D. Davydov, Ionic transport through ion-exchange and bipolar membranes. *Journal of Membrane Science* **259**, 110-121 (2005); published online EpubAug 15 (Doi 10.1016/J.Memsci.2005.03.010).
68. A. M. Deml, A. L. Bunge, M. A. Reznikov, A. Kolessov, R. P. O'Hayre, Progress toward a solid-state ionic field effect transistor. *J Appl Phys* **111**, (2012); published online EpubApr 1 (Artn 074511 Doi 10.1063/1.3702442).
69. S. M. Sze, Citation Classic - Physics of Semiconductor-Devices. *Cc/Eng Tech Appl Sci*, 28-28 (1982).
70. E. Stavrinidou, P. Leleux, H. Rajaona, D. Khodagholy, J. Rivnay, M. Lindau, S. Sanaur, G. G. Malliaras, Direct Measurement of Ion Mobility in a Conducting Polymer. *Advanced Materials*, n/a-n/a (2013)10.1002/adma.201301240).
71. T. J. Peckham, J. Schmeisser, M. Rodgers, S. Holdcroft, Main-chain, statistically sulfonated proton exchange membranes: the relationships of acid concentration and proton mobility to water content and their effect upon proton conductivity. *Journal of Materials Chemistry* **17**, 3255-3268 (2007)10.1039/b702339a).
72. A. C. C. Yang, R. Narimani, Z. Zhang, B. J. Frisken, S. Holdcroft, Controlling Crystallinity in Graft Ionomers, and Its Effect on Morphology, Water Sorption, and Proton Conductivity of Graft Ionomer Membranes. *Chemistry of Materials* **25**, 1935-1946 (2013); published online Epub2013/05/14 (10.1021/cm4005932).
73. T. B. Flanagan, F. A. Lewis, Electrode Potentials of the Palladium-Hydrogen System. *J Chem Phys* **29**, 1417-1418 (1958)Doi 10.1063/1.1744734).
74. T. Miyake, E. E. Josberger, S. Keene, Y. Deng, M. Rolandi, An enzyme logic bioprotonic transducer. *APL Materials* **3**, - (2015)doi:http://dx.doi.org/10.1063/1.4900886).
75. A. J. Bard, L. R. Faulkner, *Electrochemical methods : fundamentals and applications*. (Wiley, New York, ed. 2nd, 2001), pp. xxi, 833 p.
76. M. A. Folgado, P. Ferreira-Aparicio, A. M. Chaparro, Study of the Constrained Expansion of Nafion within the Hardware of a PEMFC. *ECS Transactions* **64**, 729-738 (2014).
77. Z. Ogumi, T. Kuroe, Z. i. Takehara, Gas permeation in SPE method II. Oxygen and hydrogen permeation through Nafion. *Journal of the Electrochemical Society* **132**, 2601-2605 (1985).

78. D. P. Wilkinson, J. Zhang, R. Hui, J. Fergus, X. Li, *Proton exchange membrane fuel cells: materials properties and performance*. (CRC Press, 2009).
79. T. B. Flanagan, F. Lewis, Electrode potentials of the palladium+ hydrogen system. *Transactions of the Faraday Society* **55**, 1409-1420 (1959).
80. S. Lorenzini, Osservazioni Intorno Alle Torpedini. *Firenze*, (1678).
81. R. Murray, The response of the ampullae of Lorenzini of elasmobranchs to electrical stimulation. *Journal of Experimental Biology* **39**, 119-128 (1962).
82. M. Camperi, T. C. Tricas, B. R. Brown, From morphology to neural information: The electric sense of the skate. *Plos Comput Biol* **3**, 1083-1096 (2007); published online EpubJun (ARTN e113 10.1371/journal.pcbi.0030113).
83. N. Sperelakis, *Cell physiology sourcebook : essentials of membrance biophysics*. (Elsevier/AP, Amsterdam ; Boston, ed. 4th, 2012), pp. xxvi, 970 p.
84. A. J. Kalmijn, Electric and magnetic field detection in elasmobranch fishes. *Science* **218**, 916-918 (1982); published online EpubNov 26 (
85. B. Waltman, Electrical properties and fine structure of the ampullary canals of Lorenzini. *Acta physiologica Scandinavica. Supplementum* **264**, 1-60 (1966).
86. R. D. Fields, The shark's electric sense. *Scientific American* **297**, 74-81 (2007).
87. B. R. Brown, Sensing temperature without ion channels. *Nature* **421**, 495-495 (2003); published online EpubJan 30 (10.1038/421495a).
88. B. R. Brown, Temperature response in electrosensors and thermal voltages in electrolytes. *J Biol Phys* **36**, 121-134 (2010); published online EpubMar (10.1007/s10867-009-9174-8).
89. R. D. Fields, K. D. Fields, M. C. Fields, Semiconductor gel in shark sense organs? *Neurosci Lett* **426**, 166-170 (2007); published online EpubOct 22 (10.1016/j.neulet.2007.08.064).
90. B. R. Brown, J. C. Hutchison, M. E. Hughes, D. R. Kellogg, R. W. Murray, Electrical characterization of gel collected from shark electrosensors. *Phys Rev E* **65**, (2002); published online EpubJun (Artn 061903 10.1103/Physreve.65.061903).
91. E. E. Josberger, Y. X. Deng, W. Sun, R. Kautz, M. Rolandi, Two-Terminal Protonic Devices with Synaptic-Like Short-Term Depression and Device Memory. *Advanced Materials* **26**, 4986-4990 (2014); published online EpubAug 6 (Doi 10.1002/Adma.201400320).
92. Z. Hemmatian, T. Miyake, Y. Deng, E. E. Josberger, S. Keene, R. Kautz, C. Zhong, J. Jin, M. Rolandi, Taking electrons out of bioelectronics: bioprotonic memories, transistors, and enzyme logic. *Journal of Materials Chemistry C*, (2015).
93. B. R. Brown, M. E. Hughes, C. Russo, Infrastructure in the electric sense: admittance data from shark hydrogels. *J Comp Physiol A* **191**, 115-123 (2005); published online EpubFeb (10.1007/s00359-004-0579-3).
94. A. Katsaounis, S. Balomenou, D. Tsiplakides, S. Brosda, S. Neophytides, C. G. Vayenas, Proton tunneling-induced bistability, oscillations and enhanced performance of PEM fuel cells. *Applied Catalysis B-Environmental* **56**, 251-258 (2005); published online EpubMar 25 (Doi 10.1016/J.Apcatb.2004.08.018).
95. S. B. Rienecker, A. B. Mostert, G. Schenk, G. R. Hanson, P. Meredith, Heavy Water as a Probe of the Free Radical Nature and Electrical Conductivity of Melanin. *The Journal of Physical Chemistry B* **119**, 14994-15000 (2015); published online Epub2015/12/03 (10.1021/acs.jpcb.5b08970).
96. A. Javey, J. Kong, *Carbon nanotube electronics*. (Springer Science & Business Media, 2009).
97. J. K. Holt, H. G. Park, Y. M. Wang, M. Stadermann, A. B. Artyukhin, C. P. Grigoropoulos, A. Noy, O. Bakajin, Fast mass transport through sub-2-nanometer carbon nanotubes. *Science* **312**, 1034-1037 (2006); published online EpubMay 19 (DOI 10.1126/science.1126298).

98. L. Sun, R. M. Crooks, Single carbon nanotube membranes: A well-defined model for studying mass transport through nanoporous materials. *J Am Chem Soc* **122**, 12340-12345 (2000); published online EpubDec 13 (Doi 10.1021/Ja002429w).
99. M. Majumder, N. Chopra, R. Andrews, B. J. Hinds, Nanoscale hydrodynamics - Enhanced flow in carbon nanotubes. *Nature* **438**, 44-44 (2005); published online EpubNov 3 (Doi 10.1038/43844a).
100. A. Noy, H. G. Park, F. Fornasiero, J. K. Holt, C. P. Grigoropoulos, O. Bakajin, Nanofluidics in carbon nanotubes. *Nano Today* **2**, 22-29 (2007); published online EpubDec (Doi 10.1016/S1748-0132(07)70170-6).
101. K. Koga, G. T. Gao, H. Tanaka, X. C. Zeng, Formation of ordered ice nanotubes inside carbon nanotubes. *Nature* **412**, 802-805 (2001); published online EpubAug 23 (Doi 10.1038/35090532).
102. T. A. Hilder, S. H. Chung, Carbon nanotube as a gramicidin analogue. *Chemical Physics Letters* **501**, 423-426 (2011); published online EpubJan 7 (DOI 10.1016/j.cplett.2010.11.034).
103. T. E. Decoursey, Voltage-gated proton channels and other proton transfer pathways. *Physiological Reviews* **83**, 475-579 (2003); published online EpubApr (Doi 10.1152/Physrev.00028.2002).
104. K. Kim, J. Geng, R. Tunuguntla, L. R. Comolli, C. P. Grigoropoulos, C. M. Ajo-Franklin, A. Noy, Osmotically-driven transport in carbon nanotube porins. *Nano Lett* **14**, 7051-7056 (2014); published online EpubDec 10 (10.1021/nl5034446).
105. R. H. Tunuguntla, M. A. Bangar, K. Kim, P. Stroeve, C. Grigoropoulos, C. M. Ajo-Franklin, A. Noy, Bioelectronic Light-Gated Transistors with Biologically Tunable Performance. *Adv Mater*, (2014); published online EpubNov 20 (10.1002/adma.201403988).
106. C. Y. Lee, W. Choi, J.-H. Han, M. S. Strano, Coherence Resonance in a Single-Walled Carbon Nanotube Ion Channel. *Science* **329**, 1320-1324 (2010); published online EpubSeptember 10, 2010 (10.1126/science.1193383).
107. H. Y. Jung, J. W. Kim, Role of the glass transition temperature of Nafion 117 membrane in the preparation of the membrane electrode assembly in a direct methanol fuel cell (DMFC). *Int J Hydrogen Energ* **37**, 12580-12585 (2012); published online EpubSep (DOI 10.1016/j.ijhydene.2012.05.121).
108. K. Atsuta, H. Suzuki, S. Takeuchi, A parylene lift-off process with microfluidic channels for selective protein patterning. *J Micromech Microeng* **17**, 496-500 (2007); published online EpubMar (Doi 10.1088/0960-1317/17/3/011).
109. B. Ilic, H. G. Craighead, Topographical Patterning of Chemically Sensitive Biological Materials Using a Polymer-Based Dry Lift Off. *Biomed Microdevices* **2**, 317-322 (2000); published online EpubDec (Doi 10.1023/A:1009911407093).
110. A. A. Puretzky, D. B. Geohegan, S. Jesse, I. N. Ivanov, G. Eres, In situ measurements and modeling of carbon nanotube array growth kinetics during chemical vapor deposition. *Appl Phys a-Mater* **81**, 223-240 (2005); published online EpubJul (DOI 10.1007/s00339-005-3256-7).